

# The velocity field of the outer Galaxy<sup>★</sup>

J. Brand<sup>1,2</sup> and L. Blitz<sup>3</sup>

<sup>1</sup> Osservatorio Astrofisico di Arcetri, Florence, Italy

<sup>2</sup> Istituto di Radioastronomia, CNR Via Irnerio 46, I-40126 Bologna, Italy

<sup>3</sup> Astronomy Department, University of Maryland College Park, MD 20742, USA

Received August 11, 1992; accepted February 11, 1993

**Abstract.** We present the velocity field of the outer Galaxy over a range in galactic longitude from  $l=90^\circ$  to  $l=270^\circ$ , out to a galactocentric radius  $R$  of about 17 kpc ( $2R_0$ ). The field also covers a region of the inner Galaxy, within 2–3 kpc from the Sun. The data set consists of a sample of H II regions/reflection nebulae, for which we have (spectro-) photometric distances, and their associated molecular clouds (for which we have radial velocities). The velocity field includes non-circular motions, and consequently can be used to derive kinematic distances of objects for which only the position and radial velocity ( $V_{\text{lsr}}$ ) are available.

Adding H I tangent point data to the sample of H II regions/reflection nebulae, the data set covers a range in  $R$  from  $R \approx 0.2R_0$  to  $R \approx 2R_0$ . For  $R_0 = 8.5$  kpc and  $\Theta_0 = 220 \text{ km s}^{-1}$ , the best fit of a rotation curve of the form  $\Theta/\Theta_0 = a_1(R/R_0)^{a_2} + a_3$  is obtained with  $a_1 = 1.00767$ ,  $a_2 = 0.0394$ , and  $a_3 = 0.00712$ . The curve is approximately flat, but the outermost points indicate a slight rise in rotational velocity. We find that Oort's constant  $A = 12.6 \text{ km s}^{-1} \text{ kpc}^{-1}$ . The mass of the Galaxy within  $R = 2R_0$  is found to be  $4.1 \cdot 10^{11} M_\odot$ .

The velocity residuals (observed  $V_{\text{lsr}}$  minus  $V_{\text{lsr}}$  expected from circular rotation) show a pattern which suggests deviations from circular rotation that are consistent with spiral density wave streaming. No clear evidence of spiral structure is seen in the *spatial* distribution of the early type stars in our sample. Streaming motions (i.e. the systematic component of the velocity residuals) are found, with a mean value of  $\approx 12 \text{ km s}^{-1}$ , implying 2-D values of  $\approx 17 \text{ km s}^{-1}$ . We find that the molecular gas is streaming past the LSR, from  $l = 180^\circ$  to  $l = 0^\circ$ , at about  $3.8 \text{ km s}^{-1}$ .

The rotation curves fitted to Northern and Southern Hemisphere data separately, are found to differ only slightly (the difference between the rotational velocities at 20 kpc being about 5%); this implies that, to first order, the galactic velocity field is axisymmetric.

From a sample of local molecular clouds (between 0.7 and 2 kpc from the Sun), we derive the height of the Sun

above the plane to be  $13 \pm 7$  pc. The scale height of these clouds is about 65 pc.

**Key words:** Galaxy: kinematics and dynamics – Galaxy: structure

## 1. Introduction

Analyses of the rotational properties of the outer Galaxy typically assume axisymmetric kinematics. Knowledge of the outer Galaxy rotation curve is usually based on data from objects in the first and second quadrant, and the assumption of an azimuthally symmetric velocity field. However, it has long been known (e.g. Burton 1966; Shane & Bieger-Smith 1966; Rickard 1968; Kerr 1969; Humphreys 1970, 1976) that there are streaming (i.e. non-circular) motions in the galactic disk, e.g. in the Perseus region (of which there is no known equivalent in the third quadrant). The velocity field of the outer Galaxy, and hence the non-circular motions, has not been adequately mapped in the third and fourth quadrant; consequently the validity of the assumption of axial symmetry should be examined, especially because a symmetric velocity field leads to a spatially asymmetric distribution of e.g. the H I gas in the Galaxy (see e.g. Henderson et al. 1982).

This paper is the first work that has reasonably complete kinematic sampling of the outer Galaxy for  $90^\circ < l < 270^\circ$  (complemented by accessible regions with  $R < R_0$ , and tangent point H I data), and therefore we can derive the full two-dimensional velocity field of the outer Galaxy. As a result, we obtain a prescription on how to correct kinematic distances from observations where only velocities are available. The velocity field is derived from a sample of H II regions and reflection nebulae, for which we have both the (spectro-) photometric distance and the velocity of the associated molecular material in which these objects are embedded. The advantage of this method over others has been discussed by Blitz (1979).

The present paper is part of a series of papers (Brand et al. 1986, hereafter Paper I; 1987, hereafter Paper II; Brand

Send offprint requests to: J. Brand (Bologna)

<sup>★</sup> Partly based on observations collected at the European Southern Observatory, Chile

& Wouterloot 1988, hereafter Paper III), that describes the various steps in the determination of the velocity field. An earlier version of this work, in slightly different form, can be found in Brand (1986).

This paper is structured as follows: in Sect. 2.1 we discuss the sample of objects (H II regions and reflection nebulae) which form the basis for the derivation of the observed velocity field, presented in Sect. 2.2. In Sect. 3 a rotation curve is fitted through the data, and various aspects of the fitting procedure, and its results, are discussed. This rotation curve is then used to derive a map of the non-circular motions in the outer Galaxy in Sect. 4. In Sect. 5 we compare the rotation curve for the northern and the southern part of our sample, and finally in Sect. 6 we look at the spatial distribution of the objects used in the derivation of the velocity field. In the following, we use the IAU-recommended values  $R_0 = 8.5$  kpc and  $\Theta_0 = 220$  km s<sup>-1</sup> (Kerr & Lynden-Bell 1986), unless stated otherwise.

## 2. The velocity field of the outer Galaxy

### 2.1. The sample

In Paper I we presented a catalogue of 400 optical H II regions and reflection nebulae, between  $l = 230^\circ$  and  $305^\circ$ , that were found by searching ESO/SRC and Palomar Observatory Sky Survey prints. Most of the objects from this list (hereafter referred to as the BBW-catalogue) were observed in CO (Paper II), and photometric distances were derived for a large number of BBW objects (Brand 1986; Paper III).

In order to derive the velocity field (and later the rotation curve), data are required that cover as large a part of the galactic disk as possible. Therefore, the BBW-sample has been supplemented with other, published data.

The one data set in the literature that contains information similar to that in the BBW-catalogue has been presented by Blitz et al. (1982; hereafter BFS). The BFS-catalogue contains galactic nebulous objects [some newly found, but mostly Sharpless regions (Sharpless 1959)] with galactic longitudes between  $l = 351^\circ$  and  $l = 360^\circ$ , and  $l = 0^\circ$  and  $l = 243^\circ$ . Blitz et al. measured CO velocities of these nebulous objects, and collected (spectro-) photometric distances from the literature for most of them. There is some overlap between the BBW- and BFS-catalogues; for objects in both catalogues, the BBW-distances were adopted, for the sake of homogeneity. For two objects (S74, S97) we used the distances determined by Forbes (1989). There are seven objects for which BFS only have a kinematic distance (Fich & Blitz 1984), but that were measured by Chini & Wink (1984). We use the latter distances in those cases, but decreased them by 25%, because Chini & Wink appear to find systematically larger distances for their objects (see Fich et al. 1989).

In the remaining sector of the Galaxy, between  $l = 305^\circ$  and  $l = 350^\circ$ , finding both photometric distances

and radial velocities of H II regions (or reflection nebulae) proves to be very difficult. There are nebulae with stellar distances (Georgelin et al. 1973; Georgelin 1975; Herbst 1975) and nebulae for which H109 $\alpha$  or CO velocities have been measured (Wilson et al. 1970; Gillespie et al. 1977; de Vries et al. 1984; Brand et al. 1984), but there is very little overlap between the two sets of data. Furthermore, in the fourth quadrant (as in the first), a particular line of sight will always sample a long length through the inner Galaxy, and usually more than one velocity component is found. In the velocity references quoted above, no attempt was made to determine which velocity component is associated with the nebula. For these reasons, no data from the Galaxy between  $l = 305^\circ$  and  $l = 350^\circ$  have been added to the data set. In this region, however, one can make use of H I (or CO) data at the tangent points, where, in the absence of abnormal streaming motions, there is a one-to-one relation between radial velocity and galactocentric distance. Here we will supplement the H II region/reflection nebula data with H I data for the inner Galaxy (kindly made available by W.B. Burton). For the data, we refer to Fich et al. (1989); their Table 2 gives the H I terminal velocities for various galactic longitudes (at  $b = 0^\circ$ ), determined with the "equivalent rectangle" method (Shane & Bieger-Smith 1966; see also Burton & Gordon 1978). Although the extreme velocities of H I profiles may be measured to accuracies substantially better than 1 km s<sup>-1</sup>, H I gas is characterized by random mass motions which lower the effective accuracy of the terminal-velocity measurements, when used for rotation curve determinations, to about 2 or 3 km s<sup>-1</sup>. We disregard the innermost part of the Galaxy (within 2 kpc from the center) because of the non-circularity of the velocities of the stars and gas (see e.g. Oort 1977).

The nebulae in this sample have been grouped into kinematically distinct complexes (i.e. nebulae close in space and velocity have been combined and appear under one set of coordinates, and one distance and velocity, representative for the complex). The complexes are listed in Table 1. The parameters of the BBW-objects were derived in Brand (1986), and have been revised for a number of objects, based on new photometric observations (Brand & Wouterloot, unpublished); the other objects (except S74 and S97) appear as listed in Fich et al. (1989). The distribution of all nebulae in Table 1, projected on the galactic plane, is shown in Fig. 1. The total range in galactocentric azimuth of the complete data set is  $110^\circ$ .

### 2.2. Two-dimensional velocity field

Figure 2a shows the observed velocity field (radial velocity  $V_{\text{lsr}}$ ) of the outer Galaxy.

The contour values range between  $-80$  and  $70$  km s<sup>-1</sup>, in steps of  $10$  km s<sup>-1</sup>. The Sun is located at  $(X, Y) = (0, 0)$  in this figure, while the galactic center is at  $(X, Y) = (0, -8.5)$ . All objects from the data set of kinematically distinct

**Table 1.** Kinematically distinct complexes

Object	Gal. long. (deg)	Gal. lat. (deg)	$d$ (kpc)	$\delta d$ (kpc)	$V_{\text{lsr}}$ (km s <sup>-1</sup> )	$\delta V$ (km s <sup>-1</sup> )	Associated objects
S8	351.36	0.61	1.70	0.30	-4.3	1.5	
S11	352.80	0.64	1.74	0.30	-3.9	1.0	
S27	4.24	22.51	0.17	0.05	3.0	1.5	
S25	5.95	-1.30	1.80	0.20	12.0	1.5	S29, 31, 32
S45	15.00	-0.68	2.20	0.20	20.0	2.0	S40, 41, 43, 44
S46	15.42	3.31	2.00	0.70	18.0	1.0	S47
S48	16.58	-0.35	2.90	0.90	44.6	1.3	
S49	17.06	0.70	2.20	0.22	24.2	2.0	
S54	18.90	2.09	2.00	0.20	27.6	0.5	
S65	29.05	-0.76	3.50	1.20	52.4	1.0	
S69	31.83	1.46	3.60	1.20	55.4	1.0	
S74	39.86	-1.23	2.10	0.80	48.1	1.8	
S82	53.56	0.04	1.10	0.40	24.0	1.0	
S86	59.66	-0.21	1.90	0.20	26.8	1.4	S87, 88, 89, 90
S90	63.12	0.44	4.00	1.30	22.2	1.0	
S93	64.14	-0.47	3.20	1.10	21.3	1.3	
S97	66.83	0.87	3.90	0.30	21.0	1.0	
S99	70.15	1.71	8.00	2.50	-22.9	2.0	S100
S101	71.59	2.76	2.50	0.80	13.7	0.4	
S104	74.79	0.57	4.40	1.40	0.0	2.0	
S112	83.78	3.28	2.10	0.70	-4.0	2.0	
S117	84.64	0.20	0.80	0.30	0.0	3.0	
S119	87.06	-4.19	0.70	0.25	3.5	1.5	
S121	90.23	1.72	4.80	1.40	-60.9	0.5	
S125	94.40	-5.57	1.00	0.16	8.0	1.0	
S124	94.57	-1.45	2.60	0.60	-43.4	1.1	
S127	96.27	2.57	7.30	2.30	-94.7	0.4	
S126	96.72	-15.14	0.60	0.20	-0.2	0.4	
S128	97.56	3.16	6.20	2.30	-72.5	0.4	
S129	99.06	7.40	0.40	0.13	-13.9	0.7	
S132	102.96	-0.80	4.20	1.50	-48.5	1.5	
S134	103.72	2.18	0.90	0.30	-16.1	0.5	
S135	104.59	1.37	1.40	0.40	-20.7	0.5	
S137	105.15	7.12	0.60	0.20	-10.3	1.4	
S139	105.77	-0.15	3.30	1.10	-46.5	0.5	
S140	106.81	5.31	0.90	0.10	-8.5	1.0	
S142	107.28	-0.90	3.40	0.30	-41.0	0.5	
S149	108.34	-1.12	5.40	1.70	-53.1	1.3	
S152	108.75	-0.93	3.60	1.10	-50.4	0.5	S153
S154	109.17	1.47	1.40	0.40	-11.5	0.9	
S156	110.11	0.05	6.40	2.00	-51.0	2.0	
S155	110.22	2.55	0.73	0.12	-10.0	1.5	
S157	111.28	-0.66	2.50	0.40	-43.0	2.0	
S158	111.54	0.78	2.80	0.90	-56.1	1.1	
S159	111.61	0.37	3.10	1.20	-56.0	1.0	
S161B	111.89	0.88	2.80	0.90	-51.9	0.7	
S162	112.19	0.22	3.50	1.10	-44.7	0.5	
S163	113.52	-0.57	2.30	0.70	-44.9	3.8	
S165	114.65	0.14	1.60	0.50	-33.0	1.0	
S168	115.79	-1.65	3.80	1.20	-40.6	1.4	
S170	117.57	2.26	2.30	0.70	-43.7	1.0	
S173	119.40	-0.84	2.70	0.90	-34.5	2.8	
S175	120.36	1.97	1.70	0.50	-49.6	0.5	
S177	120.63	-0.14	2.50	0.80	-34.2	0.4	
S184	123.04	-6.32	2.20	0.70	-30.4	1.1	
S190	133.71	1.21	2.10	0.20	-46.0	5.3	

Table 1 (continued)

Object	Gal. long. (deg)	Gal. lat. (deg)	$d$ (kpc)	$\delta d$ (kpc)	$V_{\text{lsr}}$ (km s <sup>-1</sup> )	$\delta V$ (km s <sup>-1</sup> )	Associated objects
S199	138.30	1.56	2.10	0.20	-39.0	1.0	
S202	139.99	2.09	0.80	0.30	-11.5	2.0	
S206	150.68	-0.77	3.30	0.80	-22.6	0.5	
S208	151.27	1.97	7.60	0.80	-30.2	0.4	
S209	151.61	-0.24	8.20	2.40	-52.2	2.4	
S211	154.65	2.46	5.90	1.80	-37.6	0.9	
S212	155.39	2.65	6.00	0.60	-35.3	0.3	
S217	159.15	3.27	5.20	0.80	-20.5	1.1	
S219	159.36	2.57	4.20	0.60	-24.5	1.2	
S220	160.31	-12.34	0.40	0.04	7.0	3.0	
S228	169.19	-0.90	3.50	1.10	-8.7	2.5	
S232	173.43	3.17	1.00	0.30	-23.0	0.5	
S231	173.47	2.55	2.30	0.70	-18.1	0.9	S233, 235
S234	173.48	-0.05	2.30	0.70	-13.4	0.7	
S236	173.60	-1.78	3.20	0.30	-7.2	0.5	
S237	173.97	0.25	1.80	0.30	-4.3	0.7	
S238	176.24	-20.88	0.15	0.05	8.1	0.9	S239
S241	180.79	4.03	4.70	1.20	-6.5	1.0	
S242	182.36	0.19	2.10	0.70	0.0	0.5	
S247	188.96	0.85	3.50	0.90	2.9	1.2	
S249	189.45	4.38	1.60	0.50	-5.3	2.6	
S252	189.81	0.33	1.50	0.15	7.5	1.0	
S253	192.23	3.59	4.40	0.40	14.4	0.5	
S254	192.61	-0.04	2.50	0.40	7.5	0.7	S255, 256, 257, 258
S259	192.91	-0.63	8.30	2.60	22.8	0.5	
S263	194.59	-15.74	0.45	0.14	0.3	1.0	
S269	196.45	-1.68	3.80	1.00	17.5	0.7	
S264	196.92	-10.37	0.40	0.13	12.0	0.5	
S271	197.80	-2.33	4.80	0.50	20.5	0.5	S272
S273	203.24	2.09	0.80	0.15	7.0	1.0	
S275	207.02	-1.82	1.60	0.20	14.3	0.1	
S281	208.99	-19.39	0.50	0.05	8.0	1.5	S276, 277, 278, 279
S283	210.81	-2.56	9.10	2.90	49.4	2.8	
BFS54	211.27	-0.35	8.70	2.80	21.4	0.5	
S284	211.86	-1.18	5.20	0.80	45.0	0.7	
S285	213.81	0.61	6.90	0.70	45.3	1.1	
S287	218.15	-0.35	3.20	0.80	27.2	0.8	
S288	218.77	1.95	3.00	1.20	56.7	0.8	
S292	224.10	-1.96	1.15	0.14	18.4	1.0	S293, 295, 296, 297
S294	224.19	1.22	4.60	1.50	32.9	1.1	
BBW4	228.97	-4.65	1.09	0.22	19.6	0.5	
BBW37	231.06	1.50	3.60	0.42	50.4	2.4	BBW40
BBW7A	231.51	-4.36	4.23	0.55	52.3	0.5	BBW7D
BBW6	231.57	-4.47	1.50	0.31	51.8	0.5	
BBW41	232.56	0.86	1.75	0.16	16.7	0.5	
BBW32	233.75	-0.20	3.96	0.96	44.1	0.6	
BBW50	234.58	0.83	3.08	0.70	46.7	0.5	
BBW42	234.74	-0.27	3.18	0.56	43.0	0.5	
BBW16	235.54	-4.06	1.93	0.34	28.2	2.1	
BBW33B	235.69	-1.25	5.40	2.00	74.7	0.5	
BBW29	236.60	-2.17	2.29	0.47	26.3	0.4	
BBW49	237.74	-0.96	3.02	0.52	22.3	0.5	
BBW17B	238.49	-4.66	1.35	0.08	20.6	2.2	BBW22, 23
BBW51A	239.04	-1.66	1.54	0.50	18.9	0.5	BBW51B
S310	239.65	-4.94	1.50	0.50	22.3	1.0	
BBW15	239.83	-6.52	1.73	0.35	28.2	0.5	

Table 1 (continued)

Object	Gal. long. (deg)	Gal. lat. (deg)	$d$ (kpc)	$\delta d$ (kpc)	$V_{\text{lsr}}$ (km s <sup>-1</sup> )	$\delta V$ (km s <sup>-1</sup> )	Associated objects
BBW19	240.88	-6.52	2.42	0.49	32.5	0.5	
BBW66A	241.52	-0.58	4.70	0.63	70.1	0.6	BBW66B
BBW80	243.16	0.35	4.51	0.44	49.8	0.5	
BBW98	246.01	1.26	2.52	0.51	58.0	3.6	
BBW96	246.01	1.19	6.67	1.13	59.9	3.0	BBW97
BBW110	247.47	2.19	4.04	0.82	40.8	0.2	
BBW90	247.83	-0.48	3.18	0.49	56.1	1.4	BBW92
BBW61	248.01	-5.46	4.35	0.50	51.3	0.5	
BBW101	248.90	-0.01	1.62	0.19	13.5	0.5	
BBW89	251.01	-2.82	1.79	0.37	29.2	0.2	
BBW135A	251.54	2.01	2.24	0.38	25.5	0.8	BBW135B
BBW114	251.88	-0.47	2.78	0.57	33.4	0.5	
BBW104B	252.39	-1.40	0.09	0.02	11.5	0.5	
BBW106	252.93	-1.90	1.31	0.27	10.9	0.5	
BBW146	253.58	2.23	3.85	0.79	35.9	0.5	
BBW122	253.81	-0.90	1.36	0.19	11.3	0.5	
BBW124	253.97	-0.39	2.41	0.18	35.1	1.0	BBW125A, 127, 133
BBW125B	254.06	-0.56	7.73	1.58	34.7	0.5	
BBW138	254.68	0.22	11.43	2.33	68.2	0.3	
BBW95	255.42	-4.46	0.79	0.08	9.6	0.5	BBW102
BBW109	255.42	-3.04	2.69	0.55	5.1	0.7	
BBW121	255.68	-2.27	0.33	0.07	9.4	0.5	
BBW56	255.83	-10.44	0.25	0.02	-3.9	1.1	
BBW119	255.83	-2.60	0.64	0.13	9.8	0.5	
BBW167	255.92	3.99	2.64	0.54	-16.1	0.5	
BBW143A	258.31	-1.96	0.51	0.10	8.9	1.0	
BBW129	259.24	-3.66	0.59	0.05	9.4	0.5	BBW132
BBW11	259.56	-16.48	0.23	0.05	3.6	0.5	
BBW141A	259.57	-2.82	1.85	0.20	10.0	0.5	BBW141B, C, E, F, G, J
BBW160	260.06	0.55	0.95	0.09	7.1	1.4	BBW165, 166, 169, 172
BBW93	260.38	-7.99	2.00	0.41	3.0	0.5	
BBW149	260.49	-2.54	2.49	0.51	8.1	1.5	
BBW176	261.38	0.84	0.72	0.07	4.9	0.8	
BBW173	261.47	0.32	1.21	0.25	7.5	0.5	
BBW184	262.09	1.17	0.70	0.14	7.9	0.5	
BBW177	262.18	0.36	0.40	0.08	8.2	0.5	
BBW159	262.86	-2.41	0.62	0.03	8.7	3.0	
BBW192D	263.11	1.61	1.20	0.24	5.4	0.5	
BBW182	263.56	-0.10	2.12	0.21	7.1	3.6	BBW183, 185, 186
BBW205	264.08	1.51	2.87	0.63	7.1	0.6	BBW206B
BBW206C	264.70	1.45	0.61	0.06	6.7	0.5	BBW210, 214, 215
BBW162	266.07	-4.30	1.51	0.31	5.0	0.5	
BBW137	266.20	-7.79	0.36	0.08	3.1	0.5	BBW139
BBW187B	266.47	-2.02	4.83	0.99	23.8	0.5	
BBW201	266.98	-1.27	0.77	0.16	2.1	0.5	
BBW237	267.95	1.81	0.52	0.08	-0.9	0.5	
BBW195A	268.16	-2.70	1.47	0.21	13.0	2.3	
BBW193B	268.45	-1.90	1.51	0.13	1.4	0.8	BBW194, 213, 223, 224
BBW227	268.59	-0.61	0.78	0.16	4.7	2.2	
BBW235	268.86	0.53	0.65	0.13	0.8	1.5	
BBW236	270.02	-0.51	0.61	0.12	1.9	0.5	
BBW246	270.13	0.85	3.40	0.69	9.8	1.6	
BBW239	270.43	-0.27	1.07	0.22	2.1	0.5	
BBW247	270.82	0.69	1.36	0.28	5.4	2.4	
BBW268	271.22	4.98	0.74	0.15	-2.6	0.6	
BBW255	271.23	0.96	0.53	0.11	0.6	0.5	

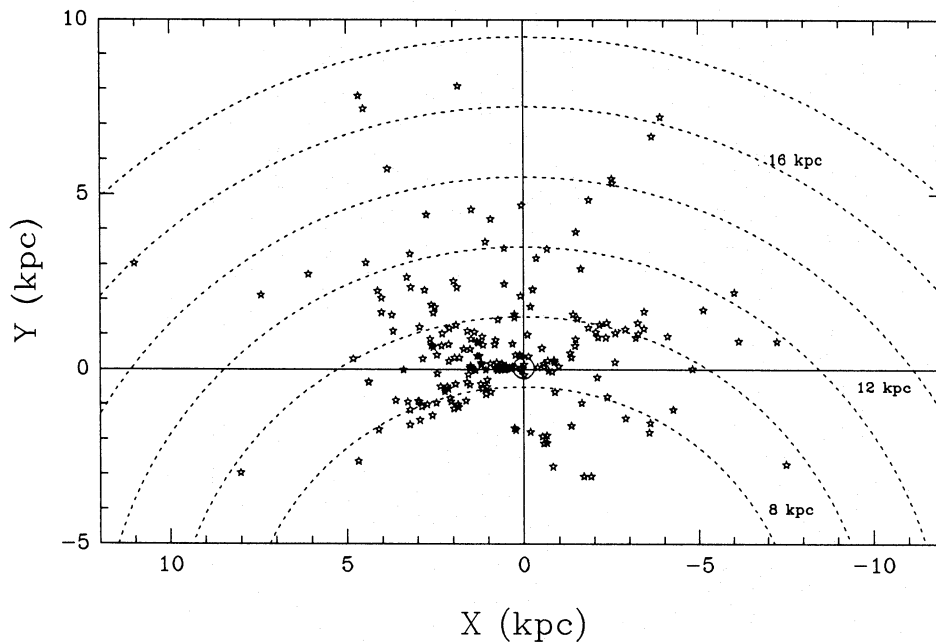


Table 1. (continued)

Object	Gal. long. (deg)	Gal. lat. (deg)	$d$ (kpc)	$\delta d$ (kpc)	$V_{\text{lsr}}$ (km s <sup>-1</sup> )	$\delta V$ (km s <sup>-1</sup> )	Associated objects
BBW240	272.83	-2.34	2.45	0.50	6.5	0.5	
BBW264	274.70	-1.47	4.41	0.90	3.1	0.5	
BBW265	275.57	-2.20	1.57	0.32	3.2	0.5	
BBW281A	281.83	-2.06	2.40	0.34	-7.0	0.5	BBW281B
BBW288	282.35	-1.39	1.97	0.40	-18.0	0.5	
BBW285	282.71	-2.48	2.22	0.49	-17.6	0.5	
BBW283	282.88	-3.14	1.64	0.15	-3.1	0.5	
BBW287	283.76	-3.41	3.73	0.76	-0.7	0.5	
BBW300B	284.30	-0.31	2.31	0.46	19.3	1.5	
BBW298	284.76	-3.06	2.21	0.24	-1.2	0.5	
BBW322A	285.87	4.44	3.42	1.06	-24.1	0.5	BBW322B
BBW316D	286.21	-0.20	2.31	0.17	-21.5	0.9	
BBW309F	286.28	-0.52	1.58	0.32	14.6	0.5	
BBW321B	286.35	3.24	1.07	0.22	-12.6	0.5	
BBW324	287.00	2.64	3.13	0.49	-13.5	0.6	BBW325
BBW311	287.22	-3.05	3.10	0.63	-7.7	0.5	
BBW314	288.97	-3.84	1.28	0.26	-13.6	0.5	
BBW323	289.78	-3.23	3.42	0.70	-14.3	0.5	
BBW328	290.34	-2.98	3.08	0.37	-12.9	0.5	
BBW347	290.35	1.62	2.91	0.34	-19.2	0.5	
BBW331	290.36	-2.84	8.55	1.74	-16.6	0.5	
BBW348A	291.29	-0.68	2.65	0.32	-24.0	0.5	
BBW353	291.94	2.06	2.23	0.45	-23.0	0.5	
BBW358	292.94	1.32	4.45	0.91	-21.8	0.5	
BBW362	294.04	-1.75	2.25	0.13	-17.9	0.5	
BBW372	295.48	0.47	1.29	0.15	-13.4	0.5	
BBW373	295.71	-0.34	1.15	0.18	-16.2	0.5	
BBW371	296.25	-3.57	3.60	0.47	-30.0	0.6	
BBW374	296.49	-2.77	3.28	0.47	-26.3	0.5	
BBW377	297.02	-1.71	2.90	0.59	-29.8	0.5	
BBW341	297.25	-15.00	0.07	0.01	4.6	0.5	
BBW382	298.42	0.69	2.11	0.43	-32.5	0.5	
BBW384	298.94	0.48	1.86	0.41	-25.7	0.5	
BBW386B	299.34	-0.29	5.37	0.60	-40.4	0.5	BBW386C, E, G BBW388
BBW387	299.57	-0.85	2.27	0.33	-35.3	1.6	
BBW396	300.53	-0.05	2.14	0.22	-22.8	0.5	
BBW399	303.66	-3.51	1.28	0.26	-23.3	0.5	
BBW400B	304.94	0.51	1.13	0.23	-35.2	1.2	

complexes are included, but they have been redistributed on a rectangular grid in  $1 \times 1$  kpc<sup>2</sup> bins, and their velocities have been averaged per bin. The new grid points around which the observed objects lie are shown as squares in Fig. 2a. For some sections of the outer Galaxy there are no objects in our data set; in order to facilitate and smooth the contouring process, we have added some points (shown as asterisks) by interpolating between the measured velocities. Because of the non-uniform distribution of grid points due to the lack of data in some parts, the contours have a certain amount of artificial structure in some places. Within 5 kpc from the Sun, for longitudes between 90° and 270°, the distribution of data points is sufficiently regular for this artificiality not to be important.

Note that the line of sight may cross a particular velocity contour more than once in the outer Galaxy (as also noted by Burton & Bania 1974a; Feitzinger & Spicker 1985). If there were purely circular rotation, this would not be so. Streaming motions are mainly responsible for this effect. Note also that in direction  $l=180^\circ$ , velocities are generally smaller than zero, while in the direction of  $l=0^\circ$ , they are positive. In both directions they should be zero, if circular rotation is assumed. This is taken as evidence that the LSR has a radial component in its motion, a confirmation of what has been found by others (see e.g. Kerr 1969; Burton & Bania 1974a; Shuter 1982; Fich et al. 1989). Non-circular motions in general will be discussed in Sect. 4.



**Fig. 1.** Projected distribution of all kinematically distinct objects from Table 1. The Sun (indicated by  $\odot$ ) is at (0, 0), the galactic center at (0, -8.5). Dotted circle segments indicate loci of points with constant galactocentric radius

Note that the distances to the H II regions in the BFS-catalogue come from a variety of sources, and therefore do *not* represent a homogeneous sample. Different authors will use, for instance, a different absolute magnitude calibration, and will consequently find a different distance, even when using the same (spectro-) photometric data (for a discussion, see e.g. Brand & Wouterloot 1988). By adopting the parameters from the BFS-catalogue, we are consistent with Fich et al. (1989) for the Northern Hemisphere part of the data. It is however wise to keep in mind the problem of an inhomogeneous set of distances, when using the plots of the observed velocity field (Figs. 2a, b) and the residuals (Fig. 10).

In the inner Galaxy, knowledge of the velocity field as derived from molecular clouds with optically visible nebulae is limited due to lack of stellar distances beyond 2 or 3 kpc from the Sun (as a result of interstellar extinction). Consequently, the velocity field we derive is limited to the outer Galaxy, and to regions of the inner Galaxy near the Sun.

The observed velocity field can be used to derive kinematic distances to molecular or H I clouds from their positions and radial velocities. To facilitate this process, the observed velocity field is again shown in Fig. 2b, with a grid superimposed, marking distances every kiloparsec for longitudes between  $0^\circ$  and  $360^\circ$ , in steps of  $5^\circ$ . Some directions in  $l$  have been labeled. This field takes into account streaming motions, and distances to objects such as H II regions in the Perseus arm will be more appropriately placed than would be the case using a simple rotation curve.

Recently, Hron (1987) determined the velocity field within 3 to 4 kpc from the Sun, using (heliocentric) radial velocity data of 105 open clusters. We have corrected his

data for the solar motion, and binned them in the same  $1 \times 1 \text{ kpc}^2$  intervals as used in Fig. 2. We find that in the 29 bins we have in common, the  $V_{\text{lsr}}$  of our H II region/molecular cloud complexes and his star clusters are within  $10 \text{ km s}^{-1}$ , twice the cloud-cloud velocity dispersion of  $5 \text{ km s}^{-1}$  (from a compilation of sources; see Sect. 4), in 72% of the cases. The mean absolute difference between the two velocities is  $9 \pm 8 \text{ km s}^{-1}$  ( $1\sigma$ ).

### 3. The rotation curve

#### 3.1. Basic equations

The rotation curve is the azimuthally smoothed average of the velocity field; it is the relation that gives the velocity of rotation in *circular orbits* with respect to the center of a galaxy, as a function of distance from this center. As such, it is a crucial piece of information in the study of such phenomena as spiral arm streaming and random motions of gas clouds. These are non-circular motions, and their analysis requires removal of the circular motions (i.e. the rotation) from the observed ones. The velocities of the stars and gas are determined by the gravitational potential, generated by the galactic mass distribution. Attacking the problem from its roots, one would start with a mass model of the Galaxy, which is adjusted such that the resulting rotation curve fits the data. For a review of this approach, see Schmidt (1983, and references therein). This is beyond the scope of this paper however, because here our primary interest is not with the mass distribution, but with the velocity field itself.

The rotation velocity of an object in the Galaxy can be given either as angular velocity,  $\omega$ , or circular velocity,  $\Theta$ . Assuming circular orbits for the gas and stars in the data

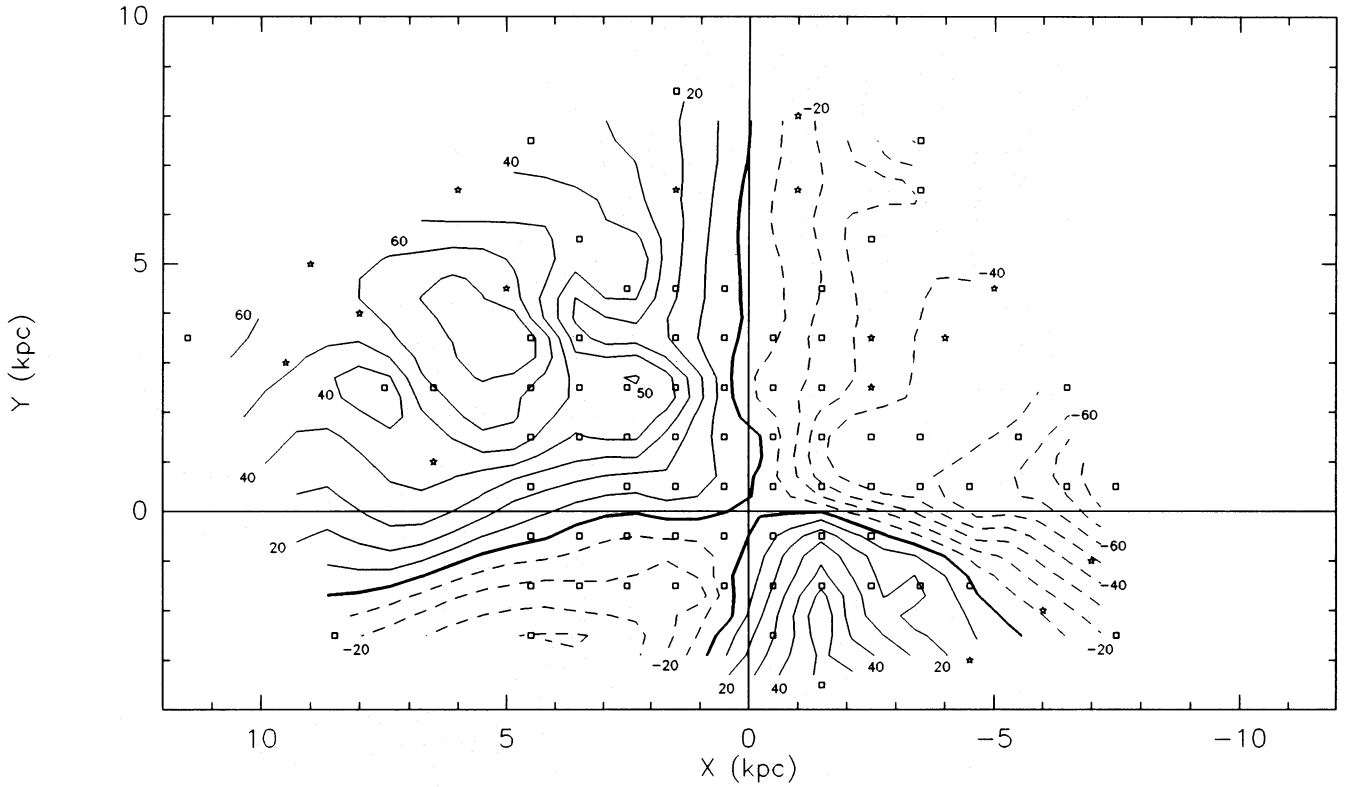


**Fig. 2a.** Observed radial velocities, projected onto the galactic plane. Location of Sun and galactic center as in Fig. 1. Contour values range from  $-80$  to  $+70 \text{ km s}^{-1}$ , in steps of  $10 \text{ km s}^{-1}$ . To obtain a smooth velocity field, velocity data were averaged in  $1 \times 1 \text{ kpc}^2$  bins (bin centers are shown as squares). For some locations in the galactic plane, data are lacking or sparse; here some points are added (shown as asterisks) through interpolation, in order to produce well-behaved contours in these regions. *The velocity field shown here includes non-circular motions*

set, the measured radial velocity  $V_{\text{lsr}}$  of a nebula, at galactic coordinates  $l$  and  $b$ , can be transformed into the circular rotation velocity through

$$V_{\text{lsr}} = \left( \frac{\Theta R_0}{R} - \Theta_0 \right) \sin l \cos b, \quad (1)$$

in which  $R$  and  $\Theta$  are respectively the galactocentric distance and the circular rotation velocity of the object, while  $R_0$  and  $\Theta_0$  are the galactocentric distance of the Sun, and the circular rotation velocity at the position of the Sun. The galactocentric distance  $R$  of an object at heliocentric distance  $d$ , and galactic coordinates  $l$  and  $b$  is

$$R = (d^2 \cos^2 b + R_0^2 - 2R_0 d \cos b \cos l)^{1/2}. \quad (2)$$

Equation (1) can be written in terms of the angular rotation velocity,  $\omega$ :

$$V_{\text{lsr}} = R_0(\omega - \omega_0) \sin l \cos b \quad (3)$$

from which follows that

$$\omega = \frac{V_{\text{lsr}}}{R_0 \sin l \cos b} + \omega_0. \quad (4)$$

Comparing Eqs. (1) and (4) we see that the uncertainty in

$\Theta$  is a combination of the uncertainties in both the heliocentric distance and the radial velocity (as well as the  $l$  and  $b$  of the center of mass of the object), whereas the uncertainty in  $\omega$  is determined only by that in  $V_{\text{lsr}}$  (and  $l$  and  $b$ ). Any functional fit of the rotation curve to the data can therefore best be done in terms of  $\omega$  versus  $R$ .

The uncertainties in the derived quantities  $\omega$  and  $R$  are denoted by respectively  $\delta_\omega$  and  $\delta_R$ , and can be expressed in terms of the uncertainties in the measured quantities  $d$ ,  $V_{\text{lsr}}$ ,  $l$ , and  $b$ .

The uncertainties in  $d$  ( $\delta_d$ ) and  $V_{\text{lsr}}$  ( $\delta_{V_{\text{lsr}}}$ ) are listed in Table 1. Those in  $l$  and  $b$  are due to the fact that in most cases we have not completely mapped the molecular cloud associated with a particular nebula, and consequently we do not know the exact location of the center of mass. Assuming the average size of a (giant) molecular cloud to be 50 pc (Blitz 1980), there is a 25 pc potential error in each direction. The uncertainties due to  $l$  and  $b$  are negligible with respect to those in the other measured quantities, however. Because the CO velocities can be measured quite accurately, the uncertainty in  $V_{\text{lsr}}$  is usually very small (less than  $1 \text{ km s}^{-1}$ , although higher values occur for some complexes; see Table 1). There is however another, and more important contribution to the  $V_{\text{lsr}}$  uncertainty, which



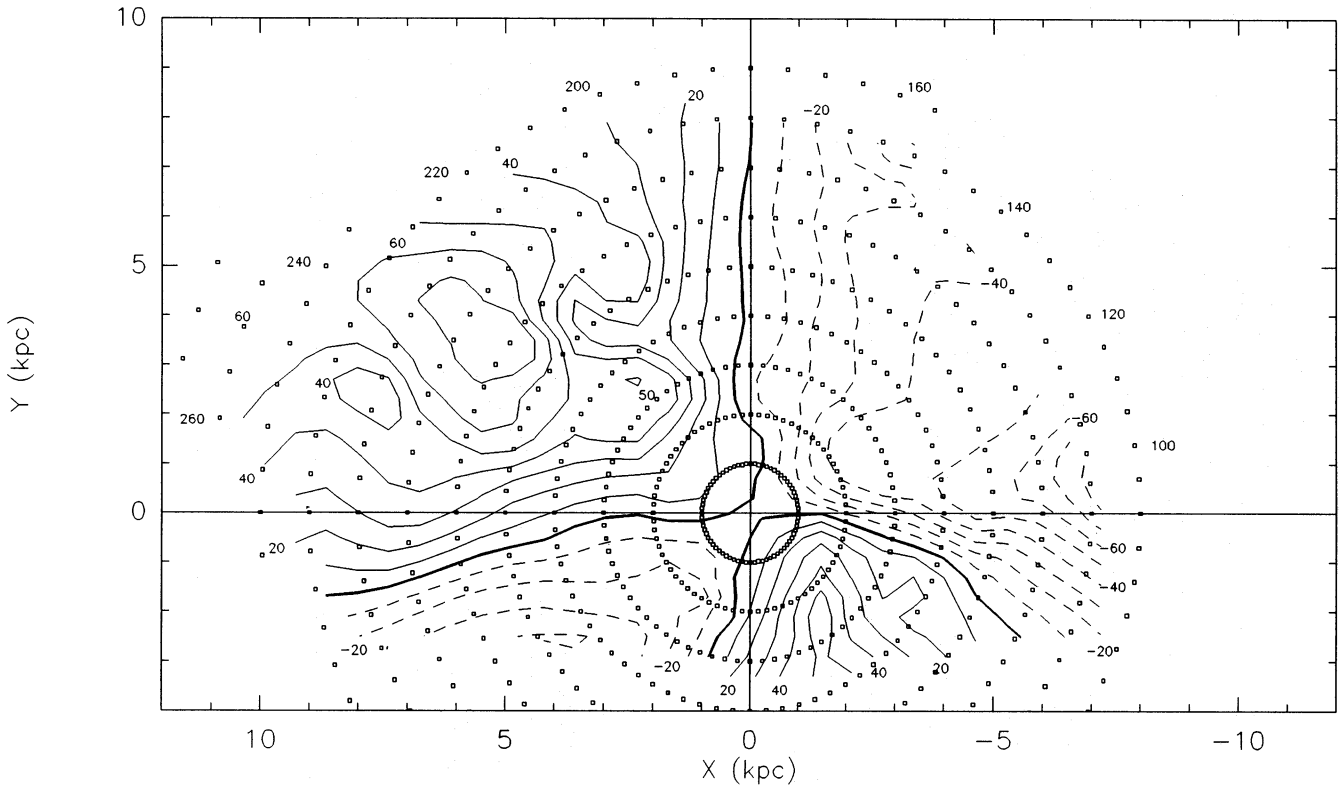


**Fig. 2b.** As Fig. 2a, but a grid has been superimposed, in which for every  $5^\circ$  in longitude distances have been marked every kiloparsec. This allows easier determination of kinematic distances for various combinations of longitude and velocity

is not due to measurement errors, but is the result of the non-circular component of the velocity of an object (both systematic and random). These extra uncertainties are not readily separable. To account for the random component, a velocity dispersion is added to the radial velocity data. A value of  $6.4 \text{ km s}^{-1}$  is assigned to this component (Blitz et al. 1980; Fich et al. 1989) and added to the measurement uncertainty in quadrature. No systematic term corresponding to the radial motion of the LSR was removed.

### 3.2. Fitting routines

To fit a rotation curve to our data, we have made use of the algorithms described in Fich et al. (1989). These authors have fitted various functions to the BFS-data, and we incorporate their results in this work.

The fitting routines we used employ a two-dimensional  $\chi^2$  fitting procedure which, unlike the standard  $\chi^2$  method, takes into account the uncertainties in both variables,  $\omega$  and  $R$ . The actual fits are made in dimensionless coordinates  $x = R/R_0$  and  $y = (\omega - \omega_0)/\omega_0$ , which have uncertainties  $\delta_x = \delta_R/R_0$  and  $\delta_y = \delta_\omega/\omega_0$ . Fich et al. have fitted a variety of functions to their data, ranging from simple polynomials like  $y = a_1 + a_2x + a_3x^2 + \dots$ , to exponentials such as  $y = a_1 + a_2e^{a_3x} + a_4e^{a_5x}$  (and combinations of polynomials and exponentials), to power laws like

$y = a_1x^{a_2-1} + a_3/x - 1$ . This last function gives good results, in the sense that it is simple, well-behaved, and provides a reasonably good fit to the data (another consideration in selecting this function is that external galaxies are found to have rotation curves with such a functional dependence; see e.g. Rubin 1983). The fitting program requires starting values for the coefficients  $a_i$  and the solar values  $R_0$ ,  $\omega_0$  and then considers points  $(x_i, y_i)$  on the curve that are closest to the data points  $(x_{di}, y_{di})$ . The closest point  $(x_i, y_i)$  is the one for which the distance  $r_i$  is minimized:

$$r_i = \frac{(y_i - y_{di})^2}{\delta_{y_{di}}^2} + \frac{(x_i - x_{di})^2}{\delta_{x_{di}}^2}.$$

The normalized sum of these  $r_i$ 's is then

$$\chi^2 = \frac{\sum_{i=1}^N r_i}{(N - n - 1)},$$

where  $N$  is the total number of data points, and  $n$  is the number of degrees of freedom. That function (or that combination of parameters for a particular function) that results in the lowest  $\chi^2$ , is recognized as the best fit to the data points. The program works by iteration, changing the previous  $a_i$ 's in every step, and stopping when the decrease

in  $\chi^2$  is smaller than a certain amount  $\varepsilon$  (which we chose to be  $10^{-4}$ ). For details of the fitting procedure, see Fich et al. (1989).

### 3.3. Results

In this section, we fit a rotation curve through the data in our sample, as listed in Table 1. Not all nebulous objects in this table are used, however. First, we eliminate objects in certain potential “problem areas”: objects within a  $30^\circ$  cone in galactic longitude, centered at  $l=0^\circ$  and  $l=180^\circ$  are left out, because for these objects the expected  $V_{\text{lsr}}$  (for circular rotation) is near zero, and the velocity uncertainty due to random motions has a large influence on the circular rotation velocity  $\Theta$ . Second, nebulae and their associated stars with  $d < 1$  kpc are also left out because, due to their small radial velocities, non-circular components in the velocity field will have a relatively large effect on their  $(\omega, R)$ -values. This leaves us with 150 objects.

Assuming  $R_0 = 8.5$  kpc and  $\Theta_0 = 220 \text{ km s}^{-1}$ , we can use Eqs. (1) and (2) to construct Fig. 3, which is the  $\Theta$  versus  $R$  diagram for the 150 objects from Table 1, that are used in the fitting procedure, and the H I data. Note that

the H I data provide information only from the tangent points, and the azimuthal averaging inherent in Fig. 3 is different for the inner and outer Galaxy.

The drawn line in Fig. 3 is the power law rotation curve fitted through the data, and will be discussed later. In Fig. 3, a distinction is made between H I and H II data (for convenience the latter term encompasses both H II regions and reflection nebulae), and between Northern Hemisphere objects ( $0^\circ \leq l < 180^\circ$ ) and Southern Hemisphere objects ( $180^\circ \leq l < 360^\circ$ ). The objects from both hemispheres have a similar range in  $\Theta$  and  $R$ .

We follow Fich et al. (1989) in their choice of the function to fit to the data. This function has the form

$$\omega/\omega_0 = a_1(R/R_0)^{a_2-1} + a_3(R_0/R). \quad (5)$$

They found that of six other functional forms, none significantly improved the fit; this power law was therefore chosen because of its simplicity. Equation (5), written as a function of  $\Theta$  is

$$\Theta/\Theta_0 = a_1(R/R_0)^{a_2} + a_3. \quad (6)$$

For clarity, the data points in Fig. 3 are plotted without error bars but there are of course uncertainties both in the  $R$  and  $\omega$ -coordinates. The uncertainty in  $\Theta$  is the combina-

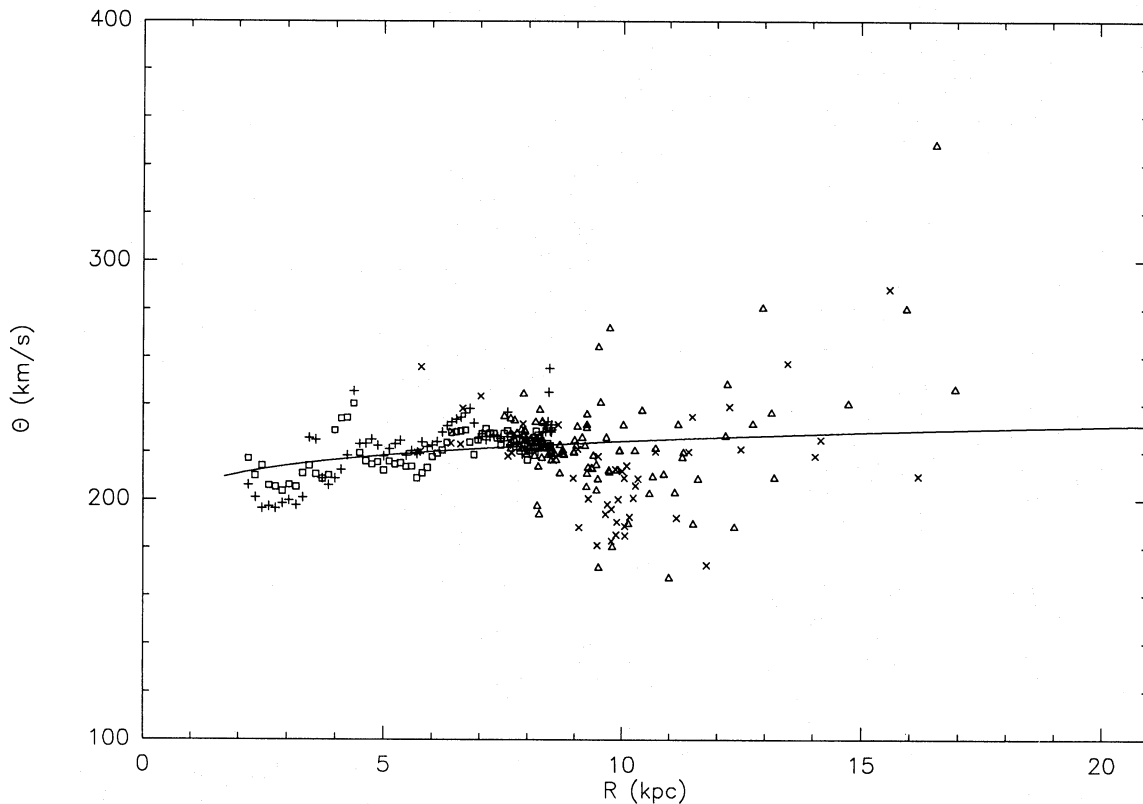


**Fig. 3.** Circular velocity  $\Theta$  as a function of galactocentric distance  $R$  for all objects used in the rotation curve fitting. The Sun is at  $(R_0, \Theta_0) = (8.5, 220)$ . Distinction is made between Northern ( $0^\circ \leq l < 180^\circ$ ) and Southern ( $180^\circ \leq l < 360^\circ$ ) Hemisphere, and H II/CO and H I data: Northern H I (plusses), Southern H I (squares), Northern H II/CO (crosses), Southern H II/CO (triangles). The drawn line is the power law rotation curve fitted through the data [see Eq. (6), with  $a_1 = 1.00767$ ,  $a_2 = 0.0394$ ,  $a_3 = 0.00712$ ]

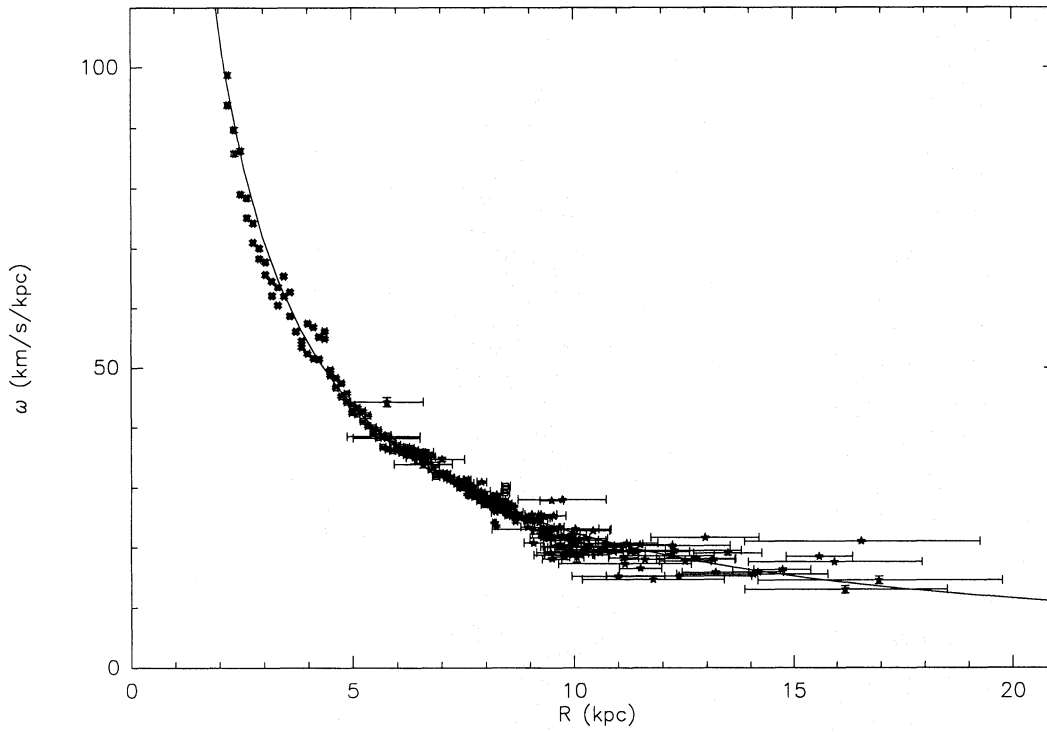


**Fig. 4a.** Angular rotation velocity  $\omega$  as a function of  $R$  for the same data as in Fig. 3. The drawn line is the power law rotation curve fitted through the data

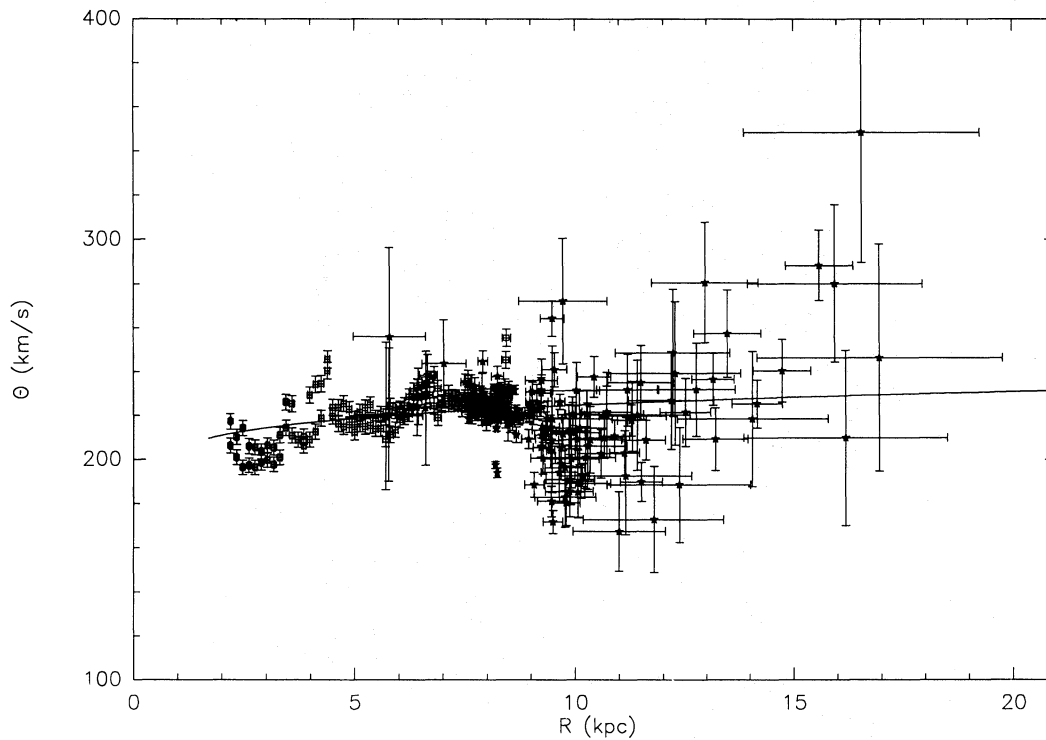


**Fig 4b.** As Fig. 3, but with error bars added. Errors in  $\Theta$  are the result of those in  $\omega$  and  $R$

tion of the uncertainties in both of these independent parameters. In fitting a rotation curve, the data points were weighted by the inverse square of their uncertainties. The H I data, too, have uncertainties, but they are generally much smaller because of the singular connection between the terminal velocities of the H I profiles and the galactocentric distance in the inner Galaxy. The H I data were weighted such that the total weight of the H I data points equals that of the H II data points. Figures 4a and b show the data points with error bars, respectively in the  $\omega$  versus  $R$ , and the  $\Theta$  versus  $R$  version. The drawn line in these panels (as in Fig. 3) is the “best fit” of the function in Eq. (5) (for Fig. 4a) or Eq. (6) (for Fig. 4b), for the solar parameters  $R_0 = 8.5$  kpc,  $\Theta_0 = 220$  km s $^{-1}$ . For this fit, the values for the parameters  $a_i$  [Eq. (5) or (6)] are  $a_1 = 1.00767$ ,  $a_2 = 0.0394$ ,  $a_3 = 0.00712$ . No random component is included in the H I velocities in Figs. 4a and b (because the H I and CO data are treated separately, this has no influence on the results).

A few things are immediately noticeable:

(i) The error bars for the H II data, especially in the outer Galaxy, are generally quite large (and almost completely due to distance uncertainties). Closer to  $R = R_0$ , the error bars are smaller. There are several reasons for this: the outer Galaxy points are mostly based on objects excit-

ed by a single star [i.e. distance uncertainties of  $\geq 25\%$ , Brand & Wouterloot (1988)], and the stars in these regions are in general faint ( $m_v > 14$ ). By eliminating objects in the “problem areas” mentioned above, objects with large error bars in  $\omega$  have been eliminated;

(ii) The mathematical form of the fitted curve does not allow it to follow all the structure in the data. As a result, at various  $R$ , groups of data points lie systematically above or below the rotation curve drawn in Fig. 4. This is attributed to streaming motions, and will be discussed in Sect. 4. A polynomial would be able to fit these deviations, but these functions are not stable at the end points (Fich et al. 1989). In any event, it would not make much sense in the present context because the fit could not then be interpreted in terms of an azimuthally smoothed rotation curve.

(iii) The H II data points in the outermost portion of the Galaxy indicate a steeper rise than what is implied by the fitted curve. The significance of this rise in rotation velocity can be illustrated by binning the data in  $R$ -intervals, and averaging  $R$  and  $\Theta$  per bin. Before averaging, weights were assigned to each point in the data set, equal to  $(1/\delta R)^2$  and  $(1/\delta \Theta)^2$  respectively, with  $\delta R$  the uncertainty in  $R$ , and  $\delta \Theta$  that in  $\Theta$ , as shown in Fig. 4b. Figure 5 shows the result of this exercise. The error bars are  $\pm 1\sigma$ .

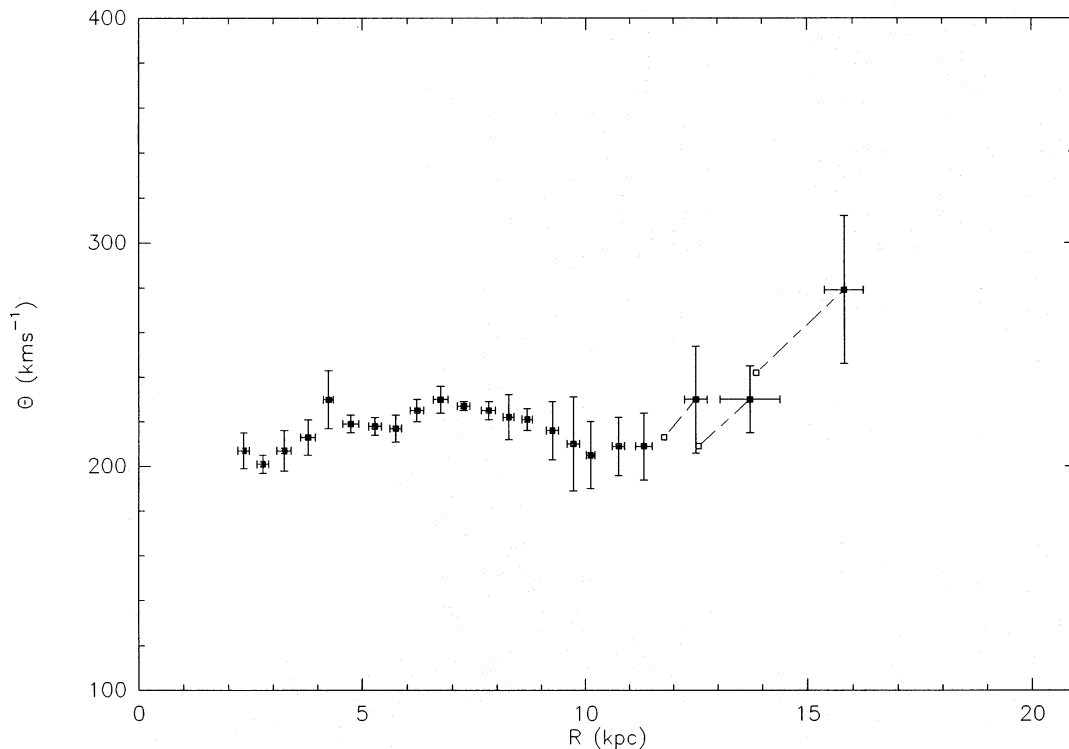


**Fig. 5.** As Fig. 4b, but with the data binned in  $R$ , and with velocities averaged. The error bars are  $\pm 1\sigma$ . Here the rise in the velocity of rotation of the outermost data points is shown to be a significant effect. The open symbols indicate how a change in  $R$ ,  $\Theta$ , due to a galactic abundance gradient, would affect the outermost data points. Indicated changes are 7% (at  $R = 12.5$  kpc), 10% ( $R = 14$  kpc), and 15% ( $R = 16$  kpc), respectively (see Hron 1989)

Each bin contains at least five objects. The last points clearly indicate a rise in velocity with galactocentric distance.

It can be argued that the outermost points could in fact have  $(R, \Theta)$ -values that are too high. Most, if not all distances in Table 1 are determined using calibration relations (e.g. absolute magnitude as a function of spectral type) for solar metal abundance. No galactic gradient in metal abundance was taken into account, which (Hron 1989) can lead to overestimating  $R$  and  $\Theta$  of the (far) outer Galaxy objects by 10% to 20%, depending on the actual value of the gradient, the galactic longitude of the object, and its “observed”  $R$ . Correcting for this effect would move the outermost points in Fig. 4b diagonally towards lower  $R$  and  $\Theta$ , thereby flattening the distribution of data points (and the rotation curve). In Fig. 5 we demonstrate the effect of this: the open symbols show the location of the outermost points for a change in  $R, \Theta$  of 7% (for  $R=12.5$  kpc), 10% (for  $R=14$  kpc), and 15% (for  $R=16$  kpc) respectively, which are the most extreme corrections postulated by Hron (1989).

Note, however, that Fich & Silkey (1991) find a galactic gradient of metal abundance that is less steep than that used by Hron (1989);

(iv) There is a group of data points (both in the Northern and the Southern Hemisphere) between  $R=9$  and 14 kpc (but the majority lie between  $R \approx 9$  and 10.5 kpc), that lie consistently below the fitted curve. In this group of points, the Northern Hemisphere objects are part of the Perseus arm, for which it has long been known that there is a velocity anomaly of about  $10 \text{ km s}^{-1}$  (and up to  $30 \text{ km s}^{-1}$ ) (Rickard 1968; Humphreys 1970, 1976); this lowers the value of  $\omega$  for these objects. The Southern Hemisphere objects in this group lie in the third quadrant at a position corresponding to the Perseus arm objects in the second quadrant, although they are not associated with any known spiral feature. This issue will be addressed in Sect. 4. Omitting these regions from the curve-fitting procedure does not change the result in a significant way.

### 3.3.1. Dependence on initial values

As mentioned above (Sect. 3.2), the fitting program requires starting values for the coefficients  $a_i$  ( $i=1, 2, 3$ ).

From Eqs. (5) and (6) it can be seen that  $a_1 + a_3 = 1$  must always hold, to ensure that  $\omega = \omega_0$  (or  $\Theta = \Theta_0$ ) at  $R = R_0$ . Inspection of Figs. 3 or 4 shows that the fitted curve does not exactly pass through  $(R_0, \Theta_0)$ , but it is very close (this is because the curve is not forced explicitly to go through that point); so in effect  $a_1 + a_3$  is very close to one, but not exactly equal. Running the program for various starting conditions shows that, even though the final  $a_i$ 's may differ each time, the rotation curve is in essence always the same for the same data set, and identical  $R_0, \Theta_0$ -values. The fit is therefore very stable. This is best illustrated by calculating two characteristics of the velocity field from the fitted rotation curve: Oort's constant  $A$ , and the slope of the  $\Theta$  versus  $R$  relation at  $R = R_0$ . For Oort's constant  $A$  we have, with Eq. (5)

$$A = -1/2R_0(d\omega/dR)_{R_0} = -1/2\omega_0[a_3 - a_1(a_2 - 1)]. \quad (7)$$

From Eq. (6) we find that the slope is

$$(d\Theta/dR)_{R_0} = a_1 a_2 \omega_0. \quad (8)$$

Table 2 gives the coefficients  $a_i$ , the values for  $A$ , the slope of  $\Theta(R)$  at  $R_0$ , and  $\Theta(R=20 \text{ kpc})$  for the rotation curves that had different starting values for the  $a_i$ 's (see also Table 3 of Fich et al. 1989 for an illustration of this). Because here  $A$  is determined from data covering a large part of the Galaxy, its value does not necessarily have to agree with the local value, i.e. as determined from data with a more limited range. Nevertheless (see Sect. 3.3.2) agreement is satisfactory.

It is seen that in all cases the result is basically the same rotation curve:  $A$ , the slope, and  $\Theta(20)$  do not change significantly from case to case. The only exception to this is perhaps the last example in Table 2: for this particular set of starting values ( $a_i=0, 0, 1$ ) the result is a flat curve, i.e. the slope is zero. However,  $\Theta(20)$  is still only 4% lower than in the other cases.

### 3.3.2. Influence of $R_0$ and $\Theta_0$

The shape of the fitted curve depends on the combination of  $(R_0, \Theta_0)$ , as demonstrated by the numbers in Table 3, where we changed  $R_0$  and  $\Theta_0$  independently. In Figs. 6a, b this dependence is shown graphically.

**Table 2.** Identical rotation curves

$a_1$	$a_2$	$a_3$	Slope ( $\text{km s}^{-1} \text{ kpc}^{-1}$ )	$A$ ( $\text{km s}^{-1} \text{ kpc}^{-1}$ )	$\Theta(20)$ ( $\text{km s}^{-1}$ )
1.0077	0.0394	0.00712	1.03	12.62	231
0.3380	0.1380	0.67788	1.21	12.54	233
0.3554	0.1158	0.65944	1.07	12.60	231
0.8541	0.0459	0.16044	1.01	12.62	231
0.1298	0.2622	0.88306	0.88	12.67	230
0.0028	0.0071	1.00259	0.00	13.01	221



**Table 3.** Rotation curves for various combinations of  $R_0$ ,  $\Theta_0$ 

$R_0$ (kpc)	$\Theta_0$ (km s <sup>-1</sup> )	$\omega_0$ (km s <sup>-1</sup> kpc <sup>-1</sup> )	Slope (km s <sup>-1</sup> kpc <sup>-1</sup> )	$A$ (km s <sup>-1</sup> kpc <sup>-1</sup> )	$\Theta(20)$
7.5	220	29.33	1.41	14.23	235
8.5	220	25.88	1.03	12.62	231
9.5	220	23.16	0.80	11.32	228
8.5	180	21.18	-1.95	11.78	170
8.5	250	29.41	3.51	13.42	285
6.5	180	27.69	-2.21	15.35	167
10.0	250	25.00	2.79	11.20	272

By making a different choice of  $R_0$ ,  $\Theta_0$  than what is used here [i.e. values different from the ones recommended by Kerr & Lynden-Bell (1986), which result in a slightly rising curve], one can produce a falling curve with the same data set. The curves are more sensitive to changes in  $\Theta_0$  than in  $R_0$ . At the same time, this does not substantially change the final value for Oort's constant  $A$ . The value of  $A$  is less sensitive to changes in  $R_0$  and  $\Theta_0$  than the slope of  $\Theta(R)$  at  $R=R_0$ . Note also, that a larger slope (i.e. a steeper rotation curve) does not imply that the curve actually follows the outermost H II points any better: changing  $R_0$  and/or  $\Theta_0$  also affects the positions of the data points in the  $\omega/R$  and  $\Theta/R$  plane! For  $R_0=8.5$  kpc and  $\Theta_0=220$  km s<sup>-1</sup> we find that  $A=12.6$  km s<sup>-1</sup> kpc<sup>-1</sup>. This gives a value for the product  $AR_0$  of 107 km s<sup>-1</sup>, which is consistent with values derived from inner Galaxy H I data (Gunn et al. 1979:  $AR_0=110\pm3$  km s<sup>-1</sup>), and CO data (McCutcheon et al. 1983:  $AR_0=103\pm5$  km s<sup>-1</sup>). Another recent determination of this product resulted in a value of  $107\pm3$  km s<sup>-1</sup> (Rohlfs et al. 1986). Schechter et al. (1988) find  $AR_0=124\pm8$  km s<sup>-1</sup>, from a sample of carbon stars. This value is outside the range of those quoted above, for reasons as yet unknown.

### 3.3.3. Comparison with previous results

An early suggestion that the galactic rotation curve for  $R>R_0$  is flatter than the extrapolation from the Schmidt curve was made by Burton & Bania (1974a), who noted that the correlation between the kinematics of the neutral and ionized hydrogen can be maximized with a flatter rotation curve. Most recent determinations of the galactic rotation curve (Jackson et al. 1979; Blitz 1979; Chini & Wink 1984; Rohlfs et al. 1986; Fich et al. 1989) use (part of) the same data set as is used in this work, so it is no surprise that all these studies find a consistent result. However, independent studies of planetary nebulae (Schneider & Terzian 1983) and neutral hydrogen (Petrovskaya & Teerikorpi 1986; Merrifield 1992) also show that the outer Galaxy rotation curve is at least flat.

We note, however, that Merrifield's (1992) analysis may suffer from various systematic errors, inherent to his

method of deriving the rotation curve from the variation of the angular thickness of the H I layer. First, the method requires the H I to move on circular orbits. As the results in his Table 1 show, there are large systematic differences between the Northern and Southern results, which suggest that there are large-scale deviations from axisymmetry in the H I. Second, additional errors in the analysis can result from the assumption of optically thin H I at all longitudes. As shown by the VLA observations of Dickey et al. (1983), it frequently happens that, even in narrow velocity ranges, the H I close to the plane of the Milky Way is optically thick, with  $\tau\approx1-2$ . Though in single-dish observations the H I is generally optically thin, there are still regions in the Galaxy (esp. near  $b=0^\circ$ ) where the neutral gas is optically thick (Burton 1992). The effect of this on Merrifield's analysis is, that the scale height at a particular value of  $W(R)$  [ $=R_0(\omega-\omega_0)$ ] will be overestimated, since the optical depth correction made by him requires  $\tau<1$ . Note that there appears to be a longitude dependence in the optical depth correction, which will affect the fitted distances. This error is likely to be a systematic effect, but because the data in Dickey et al. are too sparsely sampled, it is unclear what the actual errors will be.

Assuming that all the mass in the Galaxy is distributed in a disk with a radius of about 17 kpc (the last measured point), a slightly rising rotation curve as found here, implies a total mass of  $4.1\cdot10^{11}M_\odot$ , which is several times larger than the value derived from the Schmidt (1956, 1965) mass model, but consistent with values derived by Fich & Tremaine (1991) and Merrifield (1992). This has important implications not only for our own Galaxy (where does the mass reside?), but for the internal dynamics of the Local Group of galaxies as well. It also shows that our Galaxy is no different in this respect from other spiral galaxies (e.g. Bosma 1978; Rubin et al. 1985).

### 4. Velocity residuals and non-circular motions

The residual velocity ( $\Delta V_{\text{lsr}}$ ) of an object is defined as the difference between its observed radial velocity and the radial velocity it is expected to have according to the fitted rotation curve.

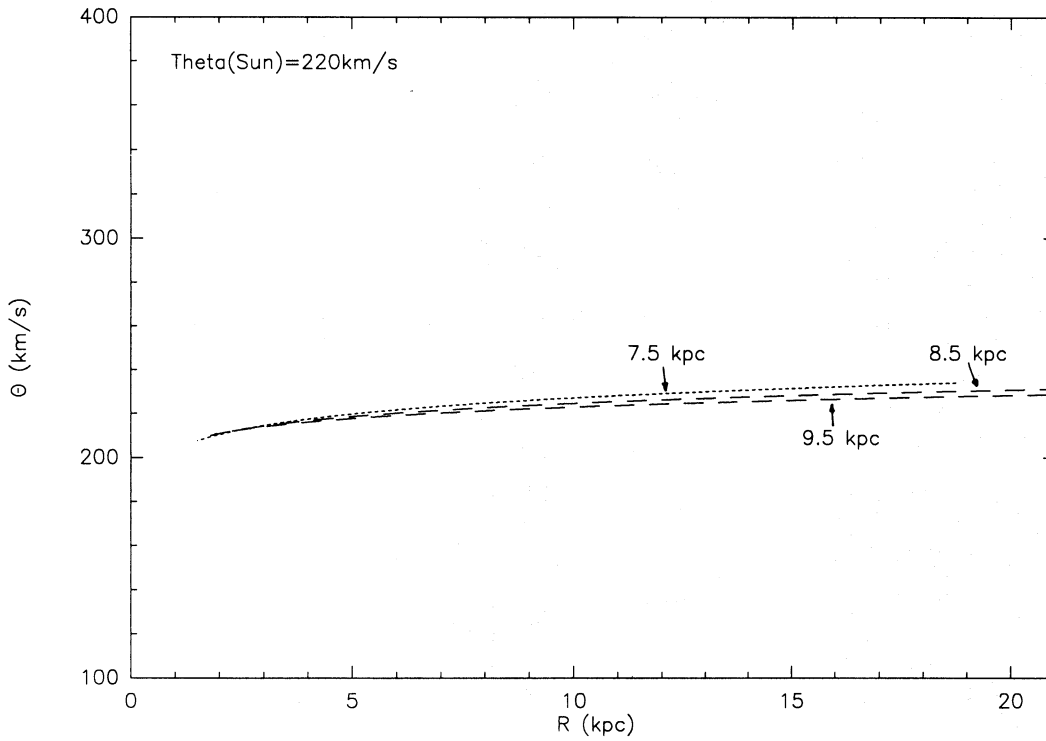


**Fig. 6a.** Rotation curves, fitted through the data, for three different values of  $R_0$  and constant  $\Theta_0 = 220 \text{ km s}^{-1}$ . A smaller value of  $R_0$  results in a slightly steeper curve

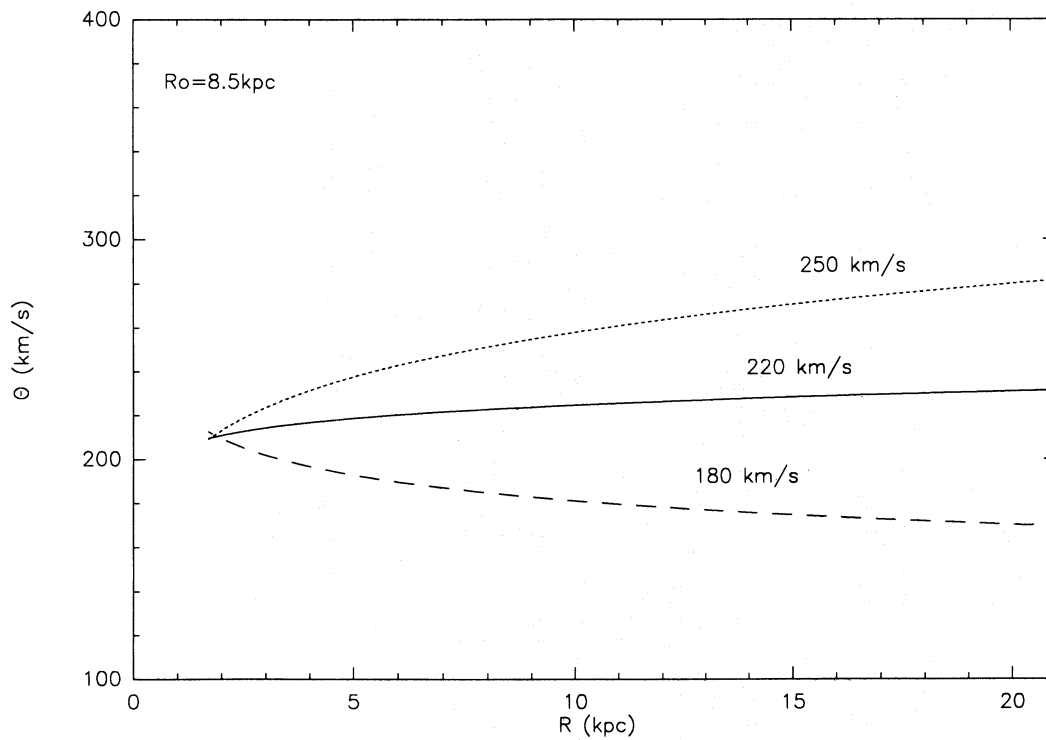


**Fig 6b.** As in Fig. 6a, but here  $R_0 = 8.5 \text{ kpc}$  in all cases, while  $\Theta_0$  varies. A higher  $\Theta_0$ -value results in a steeper rotation curve. Note that a change in  $\Theta_0$  is much more effective in changing the slope of the rotation curve than a change in  $R_0$  (cf. Fig. 6a)

The expected  $V_{\text{lsr}}$  is calculated from the power law rotation curve fitted through the data in Sect. 3.3. The radial velocity residuals as a function of longitude are plotted in Fig. 7.

The individual residuals reach (absolute) values of up to  $40 \text{ km s}^{-1}$  in some places, and are not randomly distributed. There are certain longitude ranges in which the residuals are systematically positive or negative: negative between  $l \approx 100^\circ$  and  $135^\circ$ , and between  $l \approx 275^\circ$  and  $305^\circ$  (the limit of our sample); positive between  $l \approx 225^\circ$  and  $270^\circ$ . A histogram of the residuals is shown in Fig. 8.

Because circular rotation was assumed for all objects when fitting the rotation curve, the velocity residuals reflect the presence of non-circular motions. These non-circular motions consist of a random component (the cloud-cloud velocity dispersion, denoted by  $\sigma_{\text{rand}}$ ), and a systematic component (streaming, as due to gas passing through spiral arms; denoted by  $\sigma_{\text{sys}}$ ). The random component should average to zero, when a large number of objects is observed; the systematic component might or might not average to zero when the objects in question are distributed over a large enough area of the galactic disk. For example, if the systematic component is due to spiral arm streaming, and the molecular clouds are found preferentially on one side of the arms, there may be a non-zero mean to the dispersion. In our sample, there are both a large number of objects and they cover a large fraction of the disk (206 objects with distance and velocity information, distributed as in Fig. 1); we find that  $\langle \Delta V_{\text{lsr}} \rangle = -1.3 \pm 0.9 \text{ (m.e.) km s}^{-1}$ , insignificantly different from zero. The dispersion around this average value is  $\sigma_{\text{res}} =$

$12.8 \text{ km s}^{-1}$ . This value is almost independent of the heliocentric distance of the objects (as also noted by Rohlfs et al. 1986), and is therefore not the result of measurement uncertainties, but of the degree to which the objects (i.e. the molecular clouds) follow circular rotation. Following the arguments above, one can write  $\sigma_{\text{res}}^2 = \sigma_{\text{sys}}^2 + \sigma_{\text{rand}}^2$ . The average value for  $\sigma_{\text{rand}}$ , encountered in the literature, is about  $5 \text{ km s}^{-1}$  [7: Blitz et al. (1980); 4.5: Dame (1983); 4.2: Liszt & Burton (1983); 4: Israel et al. (1984); 7–9: Stark (1984), Stark & Brand (1989); 3.0: Clemens (1985)]. This implies  $\sigma_{\text{sys}} \approx 11.8 \text{ km s}^{-1}$ , which is a one-dimensional quantity (i.e. only along the line of sight). Assuming an isotropic distribution in the galactic plane of the systematic residuals, the true  $\sigma_{\text{sys}} \approx 17 \text{ km s}^{-1}$ . This value for the systematic part of the velocity residuals compares well with what is found in external galaxies: Visser (1978) has shown (for M 81) that gas velocities can exhibit jumps of up to  $30\text{--}50 \text{ km s}^{-1}$  when the gas passes through spiral arms; Marcelin et al. (1985) find values of  $10\text{--}20 \text{ km s}^{-1}$  for these jumps (in NGC 300), while Ryden & Stark (1986) see velocity differences of up to  $30 \text{ km s}^{-1}$  for CO gas that crosses a spiral arm (in M 31). Rotation curves published by Rubin et al. (1985) and Bosma (1978) show irregularities of this order as well.

In order to see the structure in the variation with longitude of the velocity residuals more clearly, the projected distribution of all kinematically distinct complexes is shown in Figs. 9a, b, where sign and magnitude of the residuals are indicated by the symbols (see figure captions).

Figure 9a shows the projected distribution of objects with  $|\Delta V_{\text{lsr}}| \leq 5 \text{ km s}^{-1}$  ( $\approx \sigma_{\text{rand}}$ ). Clouds with a small velo-

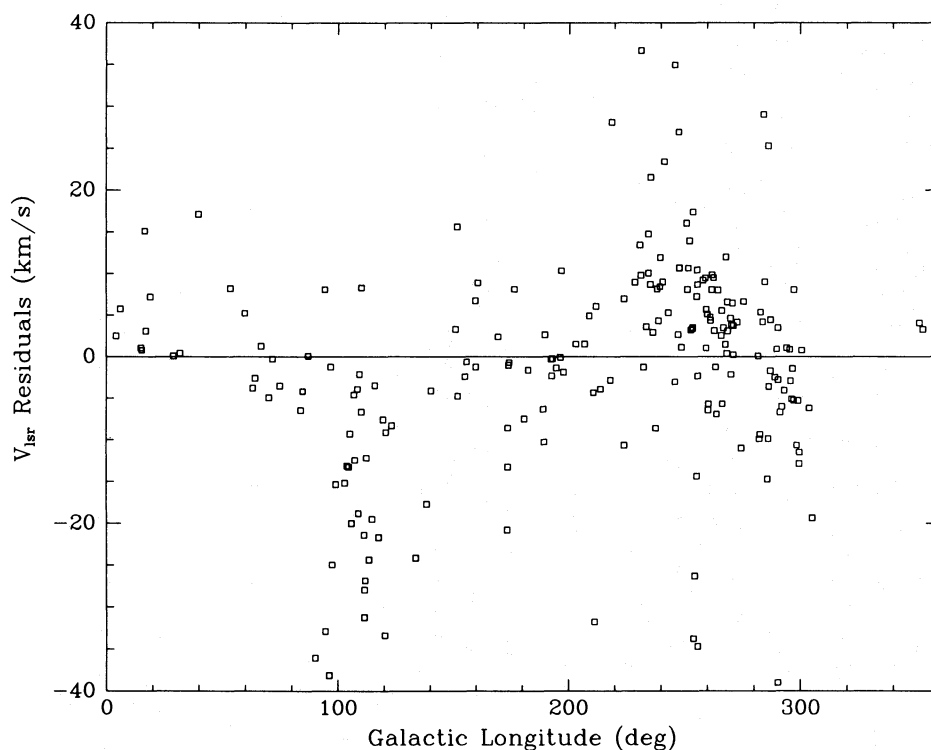


**Fig. 7.** Radial velocity residuals (observed – those expected from the rotation curve) as a function of longitude

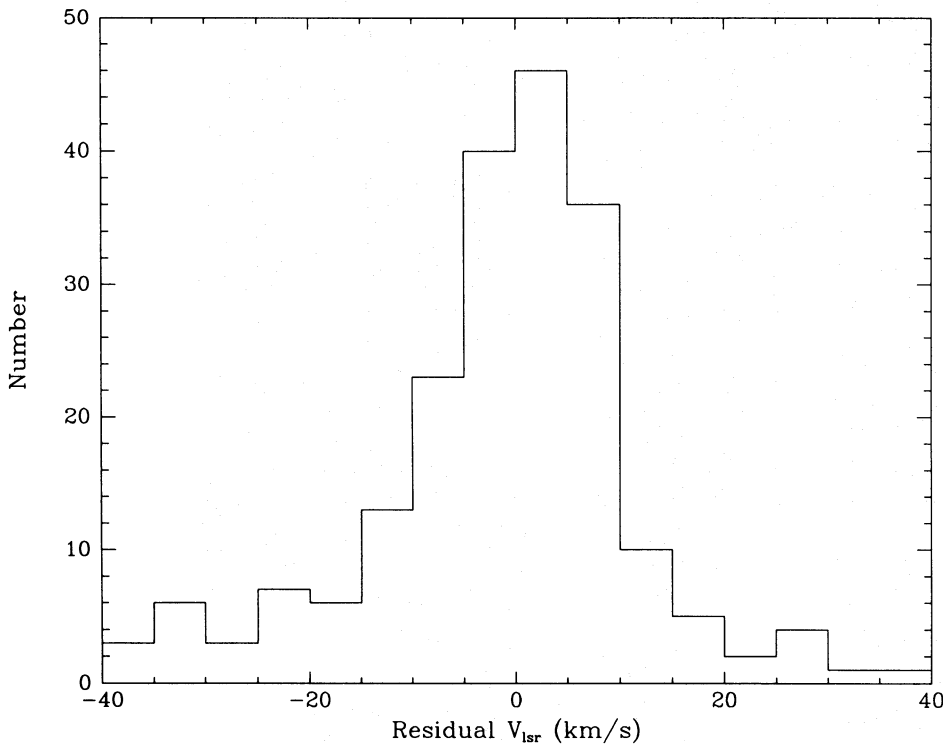


**Fig. 8.** Histogram of radial velocity residuals, in bins of  $5 \text{ km s}^{-1}$

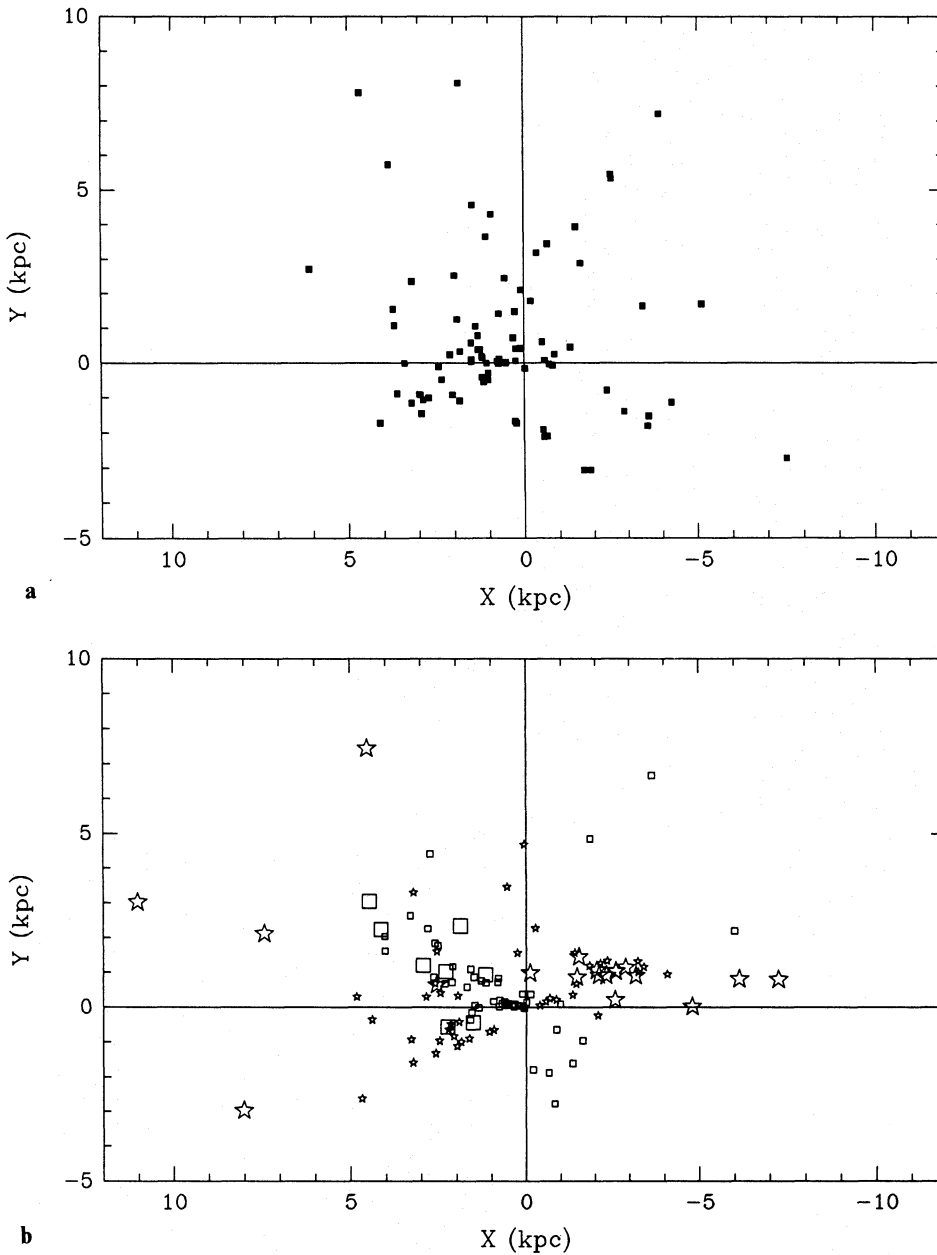
city perturbation occur uniformly in all directions that are sampled (cf. Fig. 1). In Sect. 2.2 (Fig. 2) it was noted, that the observed  $V_{\text{lsr}}$ -values towards  $l=180^\circ$  and  $l=0^\circ$  are not equal to zero, as would be expected for purely circular rotation. In fact, considering the velocity residuals of objects in a  $30^\circ$  cone, centered on these two longitudes, we find that in the direction of the anti-center  $\langle \Delta V_{\text{lsr}} \rangle = -3.8 \pm 1.8 \text{ km s}^{-1}$  (m.e.), while in the direction of the center  $\langle \Delta V_{\text{lsr}} \rangle = 3.9 \pm 0.7 \text{ km s}^{-1}$  (m.e.), which indicates there is a net motion of the molecular gas with respect to the LSR, from  $l=180^\circ$  towards  $l=0^\circ$ . Such an effect has been found by others as well (see references in Sect. 2.2). Blitz & Spergel (1991) have interpreted this motion as the result of a quadrupole term in the gravitational potential of the galactic spheroid.

Figure 9b shows the distribution of objects with larger residuals. There is a systematic trend in the sign of the residuals with position. In the second quadrant (the upper right-hand panel), the objects with negative residuals are Perseus arm regions, of which the presence of anomalous velocities was already known (Rickard 1968; Humphreys 1970, 1976). Here we see that at corresponding longitudes in the third quadrant (the upper left-hand panel), the residuals are positive; there is no known spiral feature at that location, but we may be seeing an extension of the Perseus arm.

The data points in Fig. 9b are not randomly scattered over the galactic plane. The pattern in the sign (and magnitude) of the velocity residuals is brought out more clearly in Fig. 10, which shows iso-velocity contours of the resi-

duals in steps of  $5 \text{ km s}^{-1}$ . To obtain this figure, the objects were grouped together in the same  $1 \times 1 \text{ kpc}^2$  bins as in the case of the observed velocity field (Fig. 2), and their residuals were averaged. The grid points are shown as squares. To make up for the scarcity of data in some parts of the outer Galaxy, again some points were added for which the residual velocity was obtained by interpolation. These points are indicated with an asterisk. Here, as in Fig. 2, the most reliable part of the diagram is within 5 kpc from the Sun in the outer Galaxy, and within about 2 kpc from the Sun in the inner Galaxy.

Figure 10 shows that the velocity residuals of the molecular gas are ordered on a large scale. The same is found for stars,  $\text{H II}$  gas, and  $\text{H I}$  gas (see e.g. Burton & Bania 1974a). Note that near the Sun the residuals are small and positive. This is similar to what is seen in the  $\text{H I}$  (Burton & Bania 1974b; hereafter BB). This effect has been interpreted by some as being the result of an expanding subsystem, related to Gould's belt [e.g. Lindblad et al. 1973 (and references therein); Olano 1982]. Another interpretation of the systematic velocity residuals is given by BB who show, through modeling, that the  $\text{H I}$  residuals can be reproduced in a satisfactory way by assuming that the local gas is immersed in a flow pattern as predicted by the linear density-wave theory (e.g. Lin et al. 1969). BB's Fig. 3 shows the difference between the line of sight velocity predicted by their model of the density-wave velocity field, and the circular rotation velocity field based on an extrapolation of the Schmidt (1956) rotation curve. Comparison of our Fig. 10 with BB's Fig. 3 shows an overall



**Fig. 9a and b.** Projected distribution of radial velocity residuals. The Sun is at (0,0), the galactic center at (0, -8.5). **a**  $-5 \text{ km s}^{-1} \leq \Delta V_{\text{lsr}} \leq +5 \text{ km s}^{-1}$ . **b**  $-20 \text{ km s}^{-1} \leq \Delta V_{\text{lsr}} \leq +20 \text{ km s}^{-1}$  (small asterisks),  $\Delta V_{\text{lsr}} < -20 \text{ km s}^{-1}$  (large asterisks),  $+5 \text{ km s}^{-1} < \Delta V_{\text{lsr}} \leq +20 \text{ km s}^{-1}$  (small squares),  $\Delta V_{\text{lsr}} > +20 \text{ km s}^{-1}$  (large squares)

agreement in the location of positive and negative residuals, although the details differ. The particular pattern present in the residuals will depend on the adopted location of the spiral arms, and the angle under which they cut across circles of constant galactocentric radius. The magnitude of the residuals found by BB are at most  $\pm 5 \text{ km s}^{-1}$ , which is much smaller than what is found in the present work. This would imply a stronger contrast in the arms than what was assumed in their model. Note however, that higher density in the arms and larger velocity residuals are predicted by the non-linear density-wave theory (Roberts 1969). It will be very instructive to check whether the BB model can be adjusted to reproduce the velocity residuals found here from the molecular gas. In

a discussion of the velocity structure of H I line profiles, Burton (1974) predicts the pattern and magnitude of line of sight streaming motions that are expected if all the structure in the H I profiles is of kinematic origin. His results (shown in his Fig. 4.12) agree very well with those presented here. The overall agreement between these model predictions and our findings is a good indication for organized streaming motions, as predicted by the density-wave theory, from these kinematic data.

Blitz & Spergel (1991) postulate that the gas in the Galaxy moves on elliptical orbits, in response to a triaxial spheroid. This will also give rise to velocity residuals with respect to circular rotation, but here the deviations from circular rotation should increase monotonically with  $R$ ,



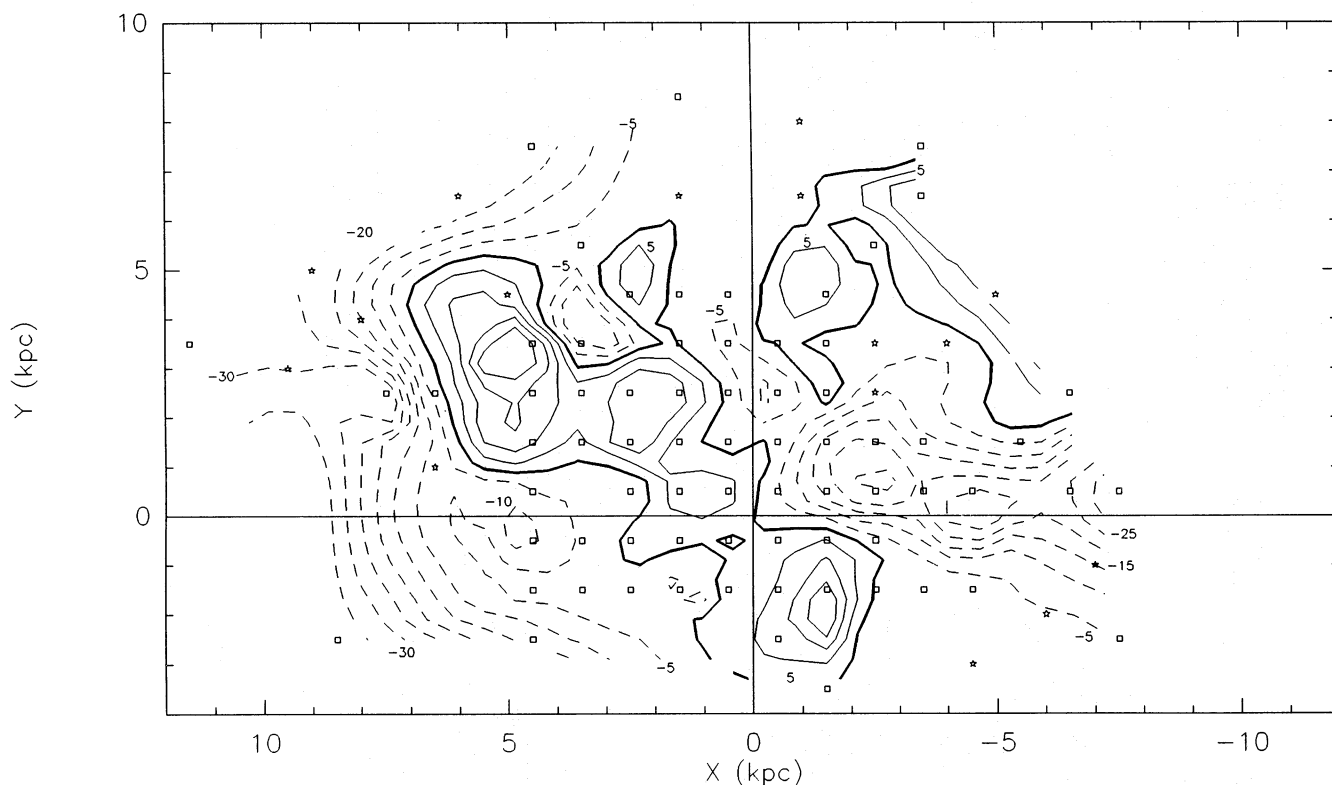


**Fig. 10.** Radial velocity residuals, projected onto the galactic plane. The Sun and the galactic center as in Fig. 1. Contour values range from  $-40$  to  $+40 \text{ km s}^{-1}$ , in steps of  $5 \text{ km s}^{-1}$ . The data were averaged in  $1 \times 1 \text{ kpc}^2$  bins (bin centers shown as squares). For some locations in the plane, points were added by interpolation (shown as asterisks)

for all longitudes, reaching a maximum difference of about  $15 \text{ km s}^{-1}$  at  $R=2R_0$ . In addition to this, only negative residuals are expected in the second quadrant, and positive ones in the third quadrant. Figure 10 shows that the residuals are ordered on a large scale in a more complex pattern, that both positive and negative values occur in each quadrant, and that these values are larger than what is predicted from the effects of elliptical streamlines. We therefore conclude that even though elliptical orbits can contribute to the residuals in Fig. 10, the detailed structure in the residual velocity field has a different origin. The most probable explanation is that it is a response to a spiral density wave. The same conclusion has been reached by others, in the case of the kinematic distribution of H I (e.g. Burton 1972; Roberts 1972; Burton & Bania 1974b).

### 5. North-south comparison

The large number of objects and their distribution in the galactic plane allow us to consider the Northern and Southern Hemisphere objects separately for a rotation curve fit. We have made separate fits to the 98 H II region- and 75 H I data points between  $0^\circ \leq l < 180^\circ$  (north), and the 52 H II region- and 75 H I data points between

$180^\circ \leq l < 360^\circ$  (south) (the same restrictions in  $l$  and  $d$  were made as for the total sample). The resulting rotation curves are shown in Fig. 11; for comparison the curve, as determined from the whole sample, is also drawn in. In all cases we used  $(R_0, \Theta_0) = (8.5 \text{ kpc}, 220 \text{ km s}^{-1})$ . The salient details of the fitted curves are summarized in Table 4.

The most striking thing about Fig. 11 is that the magnitude of the differences between the fitted rotation curves for the Southern and the Northern Hemisphere, as determined from objects in the range in galactic longitude considered by us, is no more than 5%. Furthermore, the work by Petrovskaya & Teerikorpi (1986) shows that the outer Galaxy rotation curve as determined from H I data in the first and fourth galactic quadrants is flat. Observations in the four galactic quadrants therefore indicate almost identical outer Galaxy rotation curves. An important implication of this is that the assumption of an axisymmetric velocity field for the (outer) Galaxy (as is generally made in the analysis of the outer Galaxy H I data) is justified to first order. As mentioned in the Introduction, assuming an axisymmetric velocity field results in a spatially asymmetric H I distribution in the outer Galaxy (especially evident in the first and fourth quadrant, see Fig. 1 from Henderson et al. 1982). There are small differences between the Northern and the Southern Hemisphere

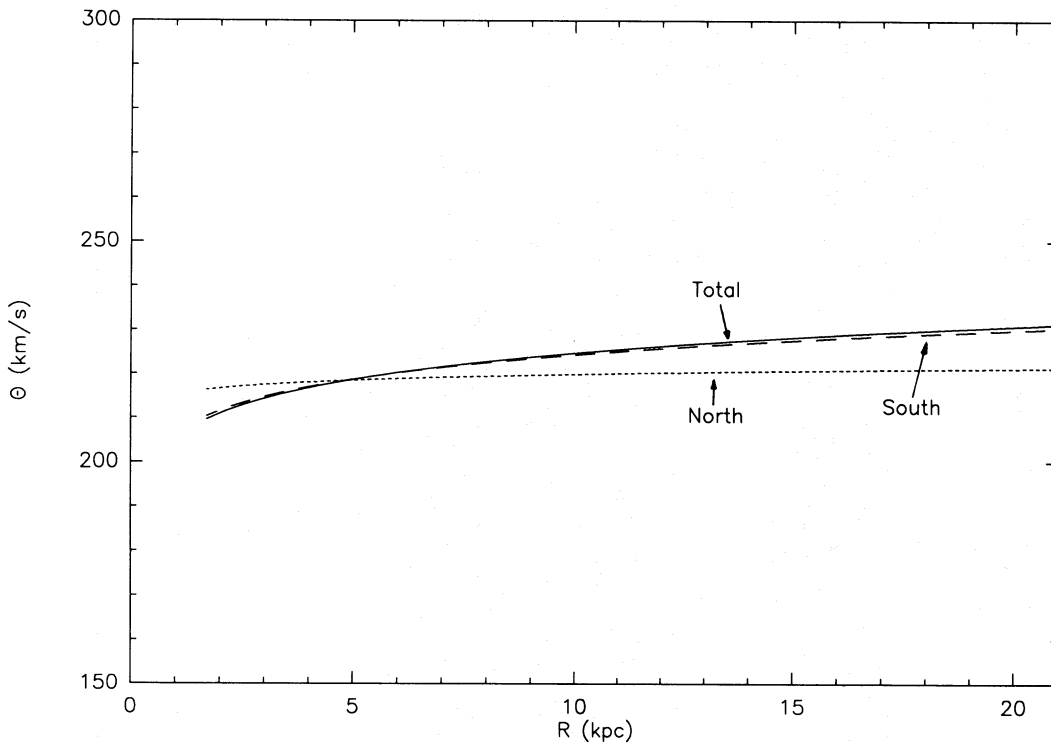


**Fig. 11.** Comparison between the Northern ( $0^\circ \leq l < 180^\circ$ ) and Southern ( $180^\circ \leq l < 360^\circ$ ) rotation curve. For reference, the curve using all available data is also shown. There are no significant differences between the curves, which implies that the smoothed velocity field is quite symmetric

**Table 4.** Comparison northern and southern rotation curves

$a_1$	$a_2$	$a_3$	Slope ( $\text{km s}^{-1} \text{ kpc}^{-1}$ )	$A$ ( $\text{km s}^{-1} \text{ kpc}^{-1}$ )	$\Theta(20)$ ( $\text{km s}^{-1}$ )	
0.9990	0.0091	-0.00099	0.24	12.80	222	North
1.0069	0.0363	0.00650	0.95	12.64	230	South
1.0077	0.0394	0.00712	1.03	12.62	231	Total sample

data (see Figs. 2, 11). Blitz & Spergel (1991) have argued that these asymmetries are due to an outward motion of the LSR, of the order of  $14 \text{ km s}^{-1}$  with respect to the  $\text{H I}$  gas at 20 kpc. The magnitude of this motion changes with  $R$ , and for nearby ( $\approx 3 \text{ kpc}$ ) molecular clouds, it is about  $4 \text{ km s}^{-1}$ , which is in fact what we find here (Sect. 4). If we correct the observed radial velocities in Table 1 for a  $4 \text{ km s}^{-1}$  motion of the LSR towards the anti-center, we find that the northern and southern curves differ by less than what is shown in Fig. 11 (see Brand 1986). In the Blitz & Spergel-model, the gas moves on triaxial orbits, which accounts for the observed spatial asymmetry in the gas distribution as well.

## 6. Spatial distribution of the nebulous objects

### 6.1. Distribution in the galactic plane

In Fig. 1 we showed the distribution of all kinematically distinct complexes (Table 1), projected onto the galactic

plane ( $b=0^\circ$ ). There is structure present in the data: in some directions one can see objects out to galactocentric radii of about  $2R_0$ . This is due to a relative lack of interstellar extinction, which in those regions of the Galaxy does not exceed 4 magnitudes (see also FitzGerald 1968; Neckel & Klare 1980; Fich & Blitz 1984). Most notable are the “fingers” at  $l \approx 95^\circ$ ,  $l \approx 150^\circ$ , and  $l \approx 215^\circ$ . In other directions, and especially in the inner Galaxy, the visibility is limited to a distance of about 3 kpc from the Sun.

Several authors have tried to discover certain (spiral arm) patterns in the distribution of  $\text{H II}$  regions. The results of these efforts are usually quite subjective, as stressed in a critical review by Liszt (1983). To see whether our  $\text{H II}$  regions would fit in such a pattern, we have selected only those regions containing at least one star of spectral type earlier than B0-B0.5, because these young stars are supposed to be found mostly in spiral arms. The projected distribution of these regions in the galactic plane is shown in Fig. 12.

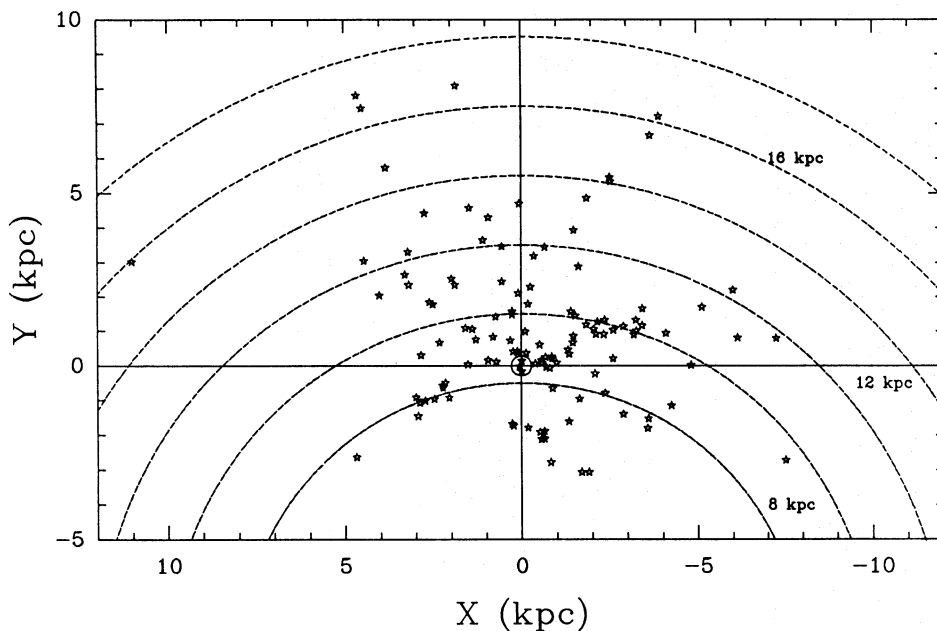


Fig. 12. Projected distribution of all kinematically distinct complexes with at least one star of spectral type earlier than B0-B0.5

It appears that the distribution of the streaming motions of the gas is a better guide to the existence of spiral structure than the spatial distribution of the stars, as suggested by comparing Fig. 12 with Fig. 10, and the discussion in Sect. 4. We note, however, that the absence of a clear spiral pattern in Fig. 12 may be the result of small-number statistics. To produce a figure of the spatial distribution comparable to Fig. 10, it would be necessary to show the *residual* surface density distribution, after subtraction of a modelled spiral arm distribution. There are not enough H II regions for a statistically significant spatial plot. Figure 12 is in fact conceptually similar to Fig. 2a, in which the velocity streaming is not readily apparent.

## 6.2. Distribution perpendicular to the galactic plane

Our data set also contains information on the distribution of the objects perpendicular to the galactic plane (the  $z$ -distribution). In Figs. 13 and 14a,c, we plotted the distribution of all kinematically distinct complexes. In Fig. 13 the  $z$ -height is shown as a function of galactocentric azimuth (defined as being zero on the Sun-center line at large  $R$  towards  $l=0^\circ$ , and  $180^\circ$  at large  $R$  towards  $l=180^\circ$ ; the azimuth lies between  $0^\circ$  and  $180^\circ$  in the first and second galactic quadrant, and between  $180^\circ$  and  $360^\circ$  in the third and fourth). The distribution in  $z$  is tilted such that for an azimuth less than  $180^\circ$  most objects lie above the plane, while the situation is reversed for azimuths larger than  $180^\circ$ .

The tilted  $z$ -distribution seen in Fig. 13 is the sign of the warp of the galactic plane (cf. Fig. 8 in Wouterloot et al. 1990). In Figs. 14a,c, the data are projected on a plane perpendicular to the plane of the Galaxy ( $z=0$ ), and containing the galactic center and the Sun.

The effect of the galactic warp is again evident, especially in the outer Galaxy. In Fig. 14a, where only objects with  $0^\circ \leq l < 180^\circ$  are shown, most objects lie above the plane  $z=0$ , while in Fig. 14c, where we plotted only objects with  $180^\circ \leq l < 360^\circ$ , most objects lie below that plane. At galactocentric distances closer to  $R_0$  the effect is less striking, although still noticeable. In Fig. 14b we show the weighted averages of  $z$ , binned in  $R$ , for objects with  $0^\circ \leq l < 180^\circ$  (i.e. those in Fig. 14a). The error bars are  $\pm 1\sigma$ . Because the four outermost bins contain a total of only 5 objects, the larger symbol at  $R=15$  kpc is the weighted average of all points with  $R > 13$  kpc. The mean  $z$ -height is significantly positive really only for the outermost points. This is comparable to Fig. 8 in Wouterloot et al. (1990), where the molecular cloud sample starts to deviate from  $z=0$  only for about  $R > 13$  kpc. Figure 14d is the equivalent of Fig. 14b for the objects with  $180^\circ \leq l < 360^\circ$ . The larger symbol at  $R=15$  kpc is again the weighted average of all (eight) objects with  $R > 13$  kpc. It must be stressed that the values plotted in Fig. 14 are averages over a large range in azimuth, and the figure should only be interpreted as a demonstration that the objects in our data set participate in the warp.

Assuming that the local nebulae and their associated molecular clouds are distributed symmetrically around  $b=0^\circ$ , one can calculate the height of the Sun above the galactic plane. However, the local sample (clouds within about 1 kpc from the Sun) may be contaminated by Gould's Belt. The Belt is a feature, mainly seen in early type stars, but Taylor et al. (1987) find that part of the local molecular cloud sample also displays a tilted distribution, which is slightly offset from the stellar Belt. The most important features in the Belt are the Ophiuchus, Taurus, and Orion regions (the first is located above the galactic plane, the other two below it). Because our data set does

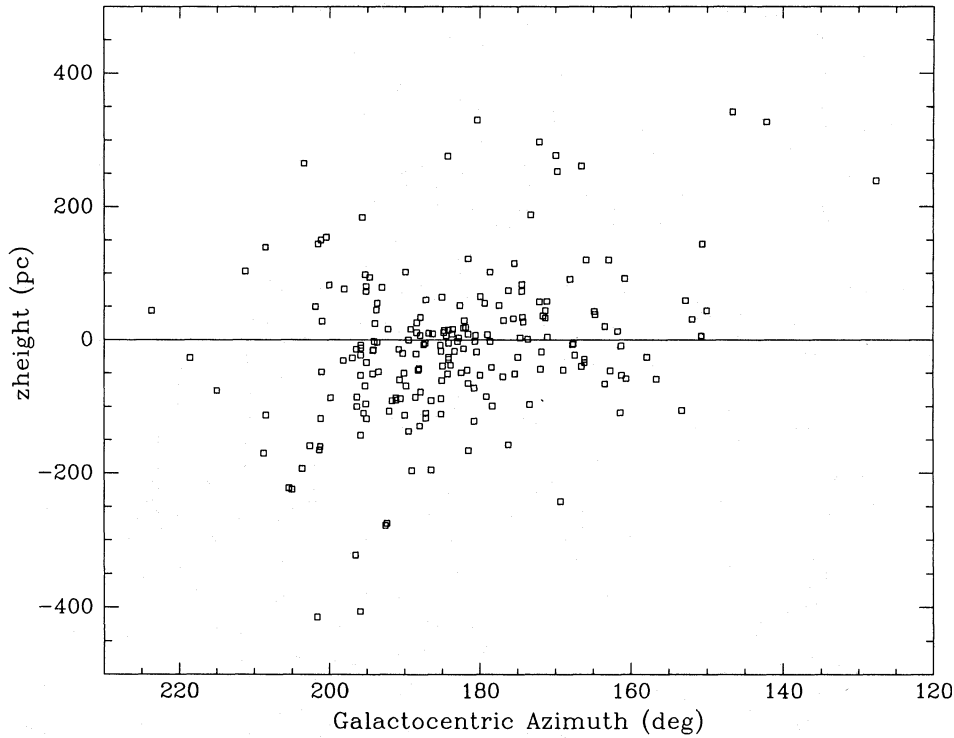


**Fig. 13.**  $z$ -Height distribution of all kinematically distinct complexes (Fig. 1 and Table 1) as a function of galactocentric azimuth. The tilt in the distribution is the sign of the galactic warp

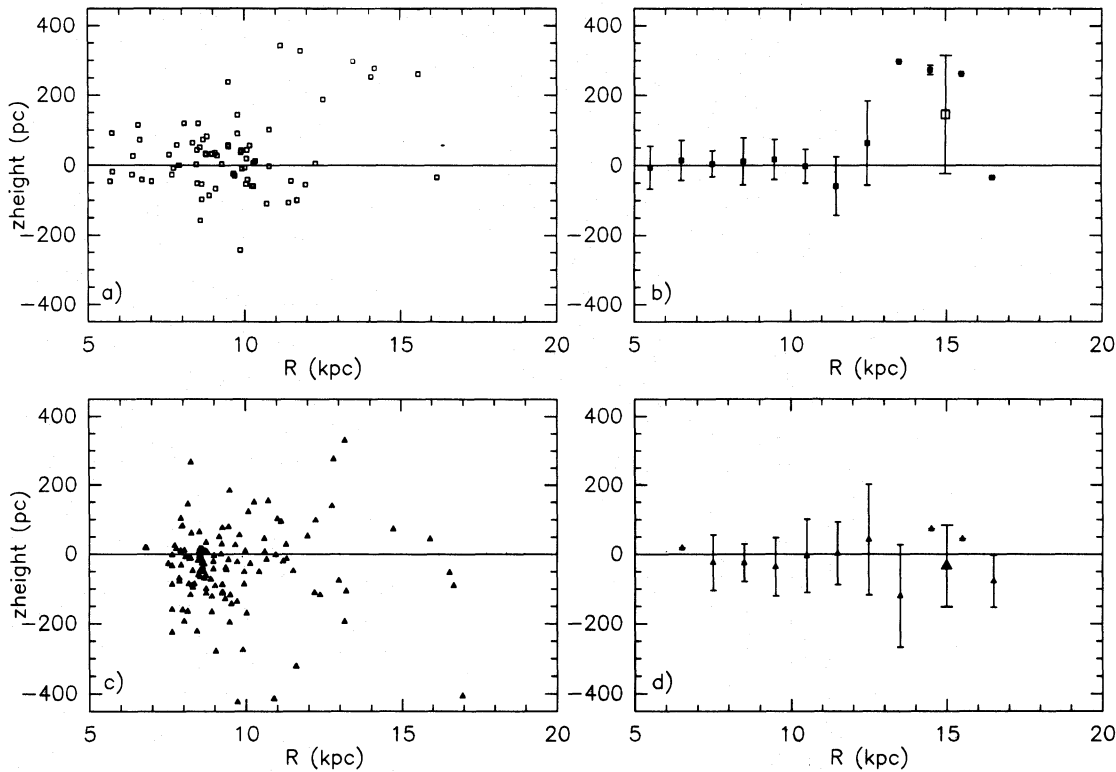


**Fig. 14.** **a**  $z$ -Height distribution of objects in the Northern Hemisphere ( $0^\circ \leq l < 180^\circ$ ). At larger  $R$ , most objects lie well above the galactic plane. Because of averaging over a large range in azimuth, more detailed information cannot be derived from this figure. **b** As **a**, but showing average  $z$ -height in bins of 1 kpc in  $R$  (smaller symbols). The larger symbol at  $R = 15$  kpc shows the average  $z$  of the 5 objects at  $R \leq 13$  kpc. The error bars are  $\pm 1\sigma$ . **c** As **a** for Southern Hemisphere ( $180^\circ \leq l < 360^\circ$ ) objects. At larger  $R$ , most objects lie below the galactic plane. **d** As **b**, but for the Southern Hemisphere objects. The larger symbol is the average  $z$ -height of the 8 objects with  $R \geq 13$  kpc

not include objects in the Ophiuchus region, while the other two lie in the galactic longitude range covered by our data, inclusion of clouds with distances inside the range of Gould's Belt objects would give a distorted distribution of  $z$ -heights. We therefore excluded objects within 0.7 kpc from the Sun (which should avoid Gould's Belt), as well as objects further away from the Sun than 2 kpc, so that the warp (and the possible incompleteness of the data for larger heliocentric distances) do not influence the distribution of the selected local clouds.

The average  $z$ -height of these (64) objects is  $\langle z \rangle = -13 \pm 7$  pc (m.e.). Assuming these local clouds are distributed symmetrically around  $b=0^\circ$ , this implies that the Sun lies slightly above the plane by  $z=13 \pm 7$  pc. This value is to be compared with values of 2 and 27 pc, respectively by Blaauw (1960; from OB stars and Cepheids), and Magnani et al. (1985; from high-latitude molecular clouds). Assuming the true distribution of the nearby clouds to be gaussian, the standard deviation of the mean  $z$ -height is found to be 55 pc, which implies a HWHM, or scale height of local molecular clouds, of about 65 pc. This number is consistent with what has been found from galactic CO surveys, which give an average gaussian scale height of  $71 \pm 16$  pc (Blitz 1991).

## 7. Conclusions

This paper presents the observed velocity field of the outer Galaxy between longitudes  $l \approx 90^\circ$  and  $l \approx 270^\circ$ , and out to  $R \approx 2R_0$ , based on a sample of H II region/reflection nebulae and their associated molecular clouds, for which independent distances and velocities are available. In the inner Galaxy, the field extends for a distance of about 2 kpc from the Sun. This velocity field includes non-circular motions, and can therefore be used to determine a kinematic distance to any object in that part of the Galaxy, as long as a radial velocity and a position are available (Sect. 2).

The data, together with inner Galaxy H I data, are used to determine the rotation curve of the Galaxy (Sect. 3). It is shown that with  $(R_0, \Theta_0) = (8.5 \text{ kpc}, 220 \text{ km s}^{-1})$  the rotation curve is slightly rising out to the last available point (roughly at  $R=2R_0$ ). Oort's constant  $A \approx 12.6 \text{ km s}^{-1} \text{ kpc}^{-1}$  in this case.

The velocity residuals (the non-circular velocity components) are studied (Sect. 4), and it is found that the molecular material is streaming past the LSR, from outer to inner Galaxy, at a velocity of about  $3.8 \text{ km s}^{-1}$ . Averaged over the whole region under study, the 2-D velocity dispersion due to streaming is about  $17 \text{ km s}^{-1}$ , in agreement with results from external galaxies. It is shown that the pattern, present in the residuals as a function of longitude and distance from the Sun, is consistent with what is expected from the influence of spiral arms on the gas.

In Sect. 5 we showed that the rotation curve determined from Southern Hemisphere objects in our sample

closely resembles that determined from Northern Hemisphere objects. To first order, the velocity field of the Milky Way is axisymmetric.

The spatial distribution of objects in our data set is discussed in Sect. 6. It is demonstrated that spiral structure is not obvious from the distribution of nebulae with early type stars alone; kinematic data are needed to deduce the presence of spiral arms. From the  $z$ -distribution of local molecular clouds, the height of the Sun above the plane of the Galaxy is found to be  $13 \pm 7$  pc, and the scale height of these clouds is about 65 pc.

*Acknowledgements.* This work is supported in part by grant no. AST89-18912 from the United States National Science Foundation. Much of the work described here was done while J.B. was employed at the Sterrewacht Leiden, The Netherlands, and the Astronomy Program at the University of Maryland, U.S.A. We have benefitted very much from discussions with, and suggestions by Drs. Jan Wouterloot and Mike Fich. Dr. W.B. Burton kindly provided the H I terminal velocities used in this work. Last but not least, J.B. thanks Loris Magnani and Sue Hoban for their hospitality during his stay in Maryland.

## References

- Blaauw A., 1960, MNRAS 121, 164
- Blitz L., 1979, ApJ 231, L115
- Blitz L., 1980, Large Scale Mapping of Local Molecular Cloud Complexes, in: Solomon P.M., Edmunds M.G. (eds.) Giant Molecular Clouds in the Galaxy. Pergamon Press, p. 1
- Blitz L., 1991, Molecular Clouds at High  $z$ , in: Bloemen H. (ed.) Proc. IAU Symp. 144, The Interstellar Disk-Halo Connection in Galaxies. Reidel, Dordrecht, p. 41
- Blitz L., Spergel D.N., 1991, ApJ 370, 205
- Blitz L., Fich M., Stark A.A., 1980, The Galactic Rotation Curve to  $R=18$  kpc, in: Andrew B.H. (ed.) Proc. IAU Symp. 87, Interstellar Molecules. Reidel, Dordrecht, p. 213
- Blitz L., Fich M., Stark A.A., 1982, ApJS 49, 183 (BFS-catalogue)
- Bosma A., 1978, Ph.D. Thesis, University of Groningen
- Brand J., 1986, Ph.D. Thesis, University of Leiden
- Brand J., Wouterloot J.G.A., 1988, A&AS 75, 177 (Paper III)
- Brand J., Blitz L., Wouterloot J.G.A., 1986, A&AS 65, 537 (BBW-catalogue; Paper I)
- Brand J., Blitz L., Wouterloot J.G.A., Kerr F.J., 1987, A&AS 68, 1 (Paper II) (Erratum in *ibid.*, 69, 343)
- Brand J., van der Bij M.D.P., de Vries C.P., et al., 1984, A&A 139, 181
- Burton W.B., 1966, Bull. Astron. Inst. Neth. 18, 247
- Burton W.B., 1972, A&A 19, 51
- Burton W.B., 1974, The Large-Scale Distribution of Neutral Hydrogen in the Galaxy, in: Verschuur G.L., Kellerman K.I. (eds.) Galactic and Extra-Galactic Radio Astronomy. Springer, Berlin, p. 82
- Burton W.B., 1992, Distribution and Observational Properties of the Interstellar Medium, in: Pfenniger D., Bartholdi P. (eds.) The Galactic Interstellar Medium. Springer, Berlin, p. 1
- Burton W.B., Bania T.M., 1974a, A&A 33, 425
- Burton W.B., Bania T.M., 1974b, A&A 34, 75 (BB)
- Burton W.B., Gordon M.A., 1978, A&A 63, 7
- Chini R., Wink J.E., 1984, A&A 139, L5



- Clemens D.P., 1985, *ApJ* 295, 422
- Dame T., 1983, Ph.D. Thesis, Columbia University
- de Vries C.P., Brand J., Israel F.P., et al., 1984, *A&AS* 56, 333
- Dickey J.M., Kulkarni S.R., van Gorkom J.H., Heiles C.E., 1983, *ApJS* 53, 591
- Feitzinger J.V., Spicker J., 1985, *MNRAS* 214, 539
- Fich M., Blitz L., 1984, *ApJ* 279, 125
- Fich M., Silkey M., 1991, *ApJ* 366, 107
- Fich M., Tremaine S., 1991, *ARA&A* 29, 409
- Fich M., Blitz L., Stark A.A., 1989, *ApJ* 342, 272
- FitzGerald M.P., 1968, *AJ* 73, 983
- Forbes D.G., 1989, *A&AS* 77, 439
- Georgelin Y.M., 1975, Ph.D. Thesis, Université de Provence
- Georgelin Y.M., Georgelin Y.P., Roux S., 1973, *A&A* 25, 337
- Gillespie A.R., Huggins P.J., Sollner T.C.L.G., et al., 1977, *A&A* 60, 221
- Gunn J.E., Knapp G.R., Tremaine S.D., 1979, *AJ* 84, 1181
- Henderson A.P., Jackson P.D., Kerr F.J., 1982, *ApJ* 263, 116
- Herbst W., 1975, *AJ* 80, 212
- Hron J., 1987, *A&A* 176, 34
- Hron J., 1989, *A&A* 222, 85
- Humphreys R.M., 1970, *AJ* 75, 602
- Humphreys R.M., 1976, *ApJ* 206, 114
- Israel F.P., de Graauw T., de Vries C.P., et al., 1984, *A&A* 134, 396
- Jackson P.D., FitzGerald M.P., Moffat A.F.J., 1979, Recent Evidence on the Rotation Curve of our Galaxy for  $R > R_0$ , in: Burton W.B. (ed.) *Proc. IAU Symp. 84, The Large-Scale Characteristics of the Galaxy*. Reidel, Dordrecht, p. 221
- Kerr F.J., 1969, *ARA&A* 7, 39
- Kerr F.J., Lynden-Bell D., 1986, *MNRAS* 221, 1023
- Lin C.C., Yuan C., Shu F.H., 1969, *ApJ* 155, 721
- Lindblad P.O., Grape K., Sandqvist A., Schober J., 1973, *A&A* 24, 309
- Liszt H.S., 1983, Determination of Galactic Spiral Structure at Radio Frequencies, in: van Woerden H., Allen R.J., Burton W.B. (eds.) *Proc. IAU Symp. 106, The Milky Way Galaxy*. Reidel, Dordrecht, p. 283
- Liszt H.S., Burton W.B., 1983,  $^{13}\text{CO}$  in the Galactic Plane: the Cloud-Cloud Velocity Dispersion in the Inner Galaxy, in: Shuter W.L.H. (ed.) *Kinematics, Dynamics and Structure of the Milky Way*. Reidel, Dordrecht, p. 135
- Magnani L., Blitz L., Mundy L., 1985, *ApJ* 295, 402
- Marcelin M., Boulesteix J., Georgelin Y.P., 1985, *A&A* 151, 144
- McCutcheon W.H., Robinson B.J., Whiteoak J.B., Manchester R.N., 1983, Distribution of CO in the southern Milky Way, in: Shuter W.L.H. (ed.) *Kinematics, Dynamics and Structure of the Milky Way*. Reidel, Dordrecht, p. 165
- Merrifield M.R., 1992, *AJ* 103, 1552
- Neckel Th., Klare G., 1980, *A&AS* 42, 251
- Olano C.A., 1982, *A&A* 112, 195
- Oort J.H., 1977, *ARA&A* 15, 295
- Petrovskaya I.V., Teerikorpi P., 1986, *A&A* 163, 39
- Rickard J.J., 1968, *ApJ* 152, 1019
- Roberts W.W., 1969, *ApJ* 158, 123
- Roberts W.W., 1972, *ApJ* 173, 259
- Rohlf K., Chini R., Wink J.E., Böhme R., 1986, *A&A* 158, 181
- Rubin V.C., 1983, Systematics of H II Rotation Curves, in: Athanassoula E. (ed.) *Proc. IAU Symp. 100, Internal Kinematics and Dynamics of Galaxies*. Reidel, Dordrecht, p. 3
- Rubin V.C., Burstein D., Ford Jr. W.K., Thonnard N., 1985, *ApJ* 289, 81
- Ryden B.S., Stark A.A., 1986, *ApJ* 305, 823
- Schechter P.L., Aaronson M., Cook K.H., Blanco V.M., 1988, Carbon Stars at  $2R_0$  and the Rotation of the Milky Way, in: Blitz L., Lockman F.J. (eds.) *The Outer Galaxy, Lecture Notes in Physics* 306. Springer, Berlin, p. 31
- Schmidt M., 1956, *Bull. Astron. Inst. Neth.* 13, 15
- Schmidt M., 1965, Rotation Parameters and Distribution of Mass in the Galaxy, in: Blaauw A., Schmidt M. (eds.) *Galactic Structure (Stars and Stellar Systems V)*. University of Chicago Press, p. 513
- Schmidt M., 1983, Models of the Mass Distribution of the Galaxy, in: van Woerden H., Allen R.J., Burton W.B. (eds.) *Proc. IAU Symp. 106, The Milky Way Galaxy*. Reidel, Dordrecht, p. 75
- Schneider S.E., Terzian Y., 1983, *ApJ* 274, L61
- Shane W.W., Bieger-Schmith G.P., 1966, *Bull. Astron. Inst. Neth.* 18, 263
- Sharpless S., 1959, *ApJS* 4, 257
- Shuter W.L.H., 1982, *MNRAS* 199, 109
- Stark A.A., 1984, *ApJ* 281, 624
- Stark A.A., Brand J., 1989, *ApJ* 339, 763
- Taylor D.K., Dickman R.L., Scoville N.Z., 1987, *ApJ* 315, 104
- Visser H.C.D., 1978, Ph.D. Thesis, University of Groningen
- Wilson T.L., Mezger P.G., Gardner F.F., Milne D.K., 1970, *A&A* 6, 364
- Wouterloot J.G.A., Brand J., Burton W.B., Kwee K.K., 1990, *A&A* 230, 21